Mobility Size and Mass of Nascent Soot Particles in a Benchmark Premixed Ethylene Flame

Joaquin Camacho*[1], Changran Liu[1], Chen Gu[2], He Lin*[2], Zhen Huang[2], Quanxi Tang[3], Xiaoqing You*[3], Chiara Saggese[4], Yang Li[5], Heejung Jung*[5], Lei Deng[6], Irenaeus Wlokas*[6], Hai Wang*[1]

[1] *Mechanical Engineering Department, Stanford University, Stanford, California 94305-3032, USA*

[2] *Key Laboratory for Power Machinery and Engineering of M.O.E, Shanghai Jiao Tong University, Shanghai 200240, China*

[3] *Center for Combustion Energy,* and *Key Laboratory for Thermal Science and Power Engineering of the Ministry of Education, Tsinghua University, Beijing 100084, China*

[4] *Department of Chemistry, Materials and Chemical Engineering "Giulio Natta", Politecnico di Milano, Piazza Leonardo da Vinci 32, 20133 Milano, Italy*

[5] *Department of Mechanical Engineering, and Center for Environmental Research and Technology (CE-CERT), College of Engineering, University of California Riverside, Riverside, California 92521, USA*

[6] *Institute for Combustion and Gasdynamics - Fluid Dynamics, University of Duisburg-Essen, 47057 Duisburg, Germany*

KEYWORDS: Soot; Mobility Sizing; Particle Size Distribution, Premixed Flames

Abstract

The burner stabilized stagnation flame technique coupled with micro-orifice probe sampling and mobility sizing has evolved into a useful tool for examining the evolution of the particle size distribution of nascent soot in laminar premixed flames. Several key aspects of this technique are examined through a multi-university collaborative study that involves both experimental measurement and computational modeling. Key issues examined include (a) data reproducibility and facility effects using four burners of different sizes and makers over three different facilities, (b) the mobility diameter and particle mass relationship, and (c) the degree to which the finite orifice flow rate affects the validity of the boundary condition in a pseudo one dimensional stagnation flow flame formulation. The results indicate that different burners across facilities yield nearly identical results after special attention is paid to a range of experimental details, including a proper selection of the sample dilution ratio and quantification of the experimental flame boundary conditions. The mobility size and mass relationship probed by tandem mass and mobility measurement shows that nascent soot with mobility diameter as small as 15 nm can deviate drastically from the spherical shape. Various non-spherical morphology models using a mass density value of 1.5 g/cm^3 can reconcile this discrepancy in nascent soot mass. Lastly, two-dimensional axisymmetric simulations of the experimental flame with and without the sample orifice flow reveals several problems of the pseudo one-dimensional stagnation flow flame approximation. The impact of the orifice flow on the flame and soot sampled, although small, is not negligible. Specific suggestions are provided as to how to treat the non-ideality of the experimental setup in experiment and model comparisons.

1. Introduction

Advances in experimental probing of sooting flames have contributed to refined theoretical and modeling studies of soot formation [1, 2]. A case in point is the use of a scanning mobility particle sizer (SMPS) and the burner-stabilized stagnation (BSS) flame sampling technique [3-6] to follow the evolution of the particle size distribution function (PSDF) of nascent soot formed in premixed flames. The BSS flame was introduced to address inherent flame perturbations occurring during probe sampling. In this technique, a stagnation surface of well-defined temperature is combined with the sampling probe. This setup enables comparisons between experimental observations and soot modeling results in a less ambiguous manner, in that the flame boundary conditions are defined and the probe itself serves as the boundary condition downstream of the flame. Using this technique, soot PSDFs have been studied in a series of flames burning a range of fuels [3-5, 7]. The results have been used in exploring chemical and physical processes of soot formation in detailed models [6, 8-11]. Among other things, the BSS flame configuration offers the advantage that the flow field of the flame may be treated more directly such that experimental and modeled PSDFs can be compared directly without having to carry out an artificial shift of any experimental or computed profiles [3].

Despite the advantages just mentioned, the accuracy of the BSS flame method coupled with probe sampling and SMPS analysis still can be impacted by several factors. These include a possible burner effect due to differences in burner size/material and how the porous plug is cooled. This can lead to variations in the heat loss to the burner and thus the maximum flame temperature, the flame position, and the preheat zone temperature gradient. Other factors include difficulties in quantifying sample dilution and its calibration during mobility measurement, how the flame gas sample is diluted and transmitted to the mobility sizer and, to an extent, the mobility sizer and its setting. The suitability to directly compare the experiment and pseudo one-dimensional (1-D) simulation also can be questionable for an otherwise 2-dimensional (2-D) flame. The far-side boundary condition applied thus far [3, 8, 10] uses zero convective velocity, whereas the actual experiment continuously extracts a small flow through the sampling orifice along the centerline of the flame.

Recent efforts have suggested that experimental observations of fundamental flame properties are the most useful when the data of overlapping experiments from several laboratories may be crosschecked to yield an assessment of the random and systematic errors (see, e.g., [12, 13]). In this spirit and to assess the accuracy of the BSS flame/SMPS technique, we report here a coordinated, collaborative effort with the goal to evaluate the uncertainty of the BSS flame technique and its sampling method on the same benchmark flame (Flame C3 of Abid et al. [3]) using facilities in three laboratories. The assessment includes, among others, three burners that differ in size and design, two SMPS component models, and two independent calibration procedures. As a tertiary objective, we also aim to make improvements to data reported by Abid et al. [3] on the same benchmark flame.

In addition to the above objectives, we report the results of direct numerical simulation of the BSS flame in a 2-D axisymmetric configuration. The flow rate at the stagnation surface is finite during soot sampling and the 2-D simulation can be used to assess this effect on the 1-D assumptions currently taken in the flame and soot models. Lastly, we note that the interpretation of the mobility size is another open question [10]. Mobility size can deviate from the true size even for a sphere [14-16] but the full extent of deviation for nascent soot has only recently been realized.

Helium ion microscopy (HIM) techniques and other related studies of nascent soot [17-19] have shed new light on the morphology nascent soot. In agreement with theoretical predictions [20, 21], nascent soot particles are hardly spherical [17, 18]. A separate diagnostic may prove to be necessary to unravel the relationship between mobility size and particle mass due to the uncertainty in the mass density of the particle material [22], structural intricacies and compositional complexity [23, 24]. This directly impacts detailed modeling because the primary size parameter that is modeled is mass and not the particle diameter. Here, we use the centrifugal particle mass analyzer (CPMA) [25, 26] to examine this relationship. In the CPMA, the balance between the electrostatic force and the so-called centrifugal force allows for particle mass to be classified independently without any knowledge about particle shape and morphology. We note that the mass-mobility relationship has been studied for larger, mature soot [27-29] but this relationship is unavailable for nascent flame soot during its size/mass growth.

In summary, mobility measurements of a benchmark flame are carried out on four different burners across three laboratories (Stanford, Shanghai Jiao Tong and Tsinghua). The mobility diameter of nascent soot is evaluated by measuring the particle mass in tandem (UC Riverside and Stanford). Lastly, DNS modeling of the experimental flame was carried out at University of Duisburg-Essen to provide a better understanding of the 2-D effects on flame modeling and to yield suggestions about how the underlying BSS flame and PSDFs of nascent soot are best modeled using the pseudo 1-D approximation.

2. Experimental

Similar mobility measurement techniques were employed across laboratories at Stanford, Tsinghua and Shanghai Jiao Tong to observe detailed sooting behavior. Key burner and experimental parameters are summarized in Table 1. Briefly, burner-stabilized flames were stabilized on respective burners at atmospheric pressure with an unburned composition of 16.3% (mol) ethylene and 23.7% (mol) oxygen in argon (Flame C3 of Abid et al. [3, 30]). The unburned gas has an equivalence ratio, ϕ, of 2.07 and a cold velocity of 8 cm/s (298 K & 1 atm).

At Stanford, two burners of different diameters (5.0 and 7.6 cm) were used to evaluate any possible burner size dependency. Unless otherwise indicated, the Stanford results are reported for measurements made with the 5.0 cm burner. The outer body of both burners is brass. The burners are water-cooled from an inner concentric channel within the burner body. The Shanghai Jiao Tong burner is a duplicate of the Stanford 5.0 cm burner. Tsinghua, on the other hand, uses a McKenna burner with a bronze porous plug 6.0 cm in diameter. Water-cooling in the McKenna burner occurs in small tubes embedded within the porous plug. In addition to the difference in the porous plug material and thickness (see, Table 1), there are other differences between the McKenna burner and the Stanford burners. Among them, the Stanford burners can have the porous plug plate replaced, whereas the McKenna burner has the porous plug plate permanently fixed into the burner housing. All flames were isolated from the ambient air by a shroud of nitrogen at a linear velocity of 25 cm/s

(298 K & 1 atm) through a concentric porous ring. The gas flows were all metered using critical orifices calibrated independently in each laboratory. The uncertainty in the flow rate is estimated to be 0.5%, mostly due to room temperature fluctuation that would impact the nozzle flow.

Temperature was measured by fine wire thermocouple coated with a Y/BeO mixture to prevent catalysis on the surface. Sizes of the coated thermocouple beads and wires are listed in Table 1. Radiation correction is carried out according to the procedure of Shaddix [31]. The gas properties were estimated by solving for flame structure and species concentrations using detailed reaction kinetics and transport [30]. Literature emissivity values for similar thermocouple coatings range from 0.3 to 0.6 [32]. Here we used the range of emissivity values to yield the upper and lower limits for the radiation correction. The radiation-corrected temperature is assumed to be the average of the two limiting values. Given that the major temperature uncertainty is from the emissivity, the uncertainty in the radiation-corrected temperatures is about ±5 K at the lowest measured temperatures and about ±90 K at the peak flame temperature. The gas temperature at the burner surface was obtained by extrapolating the axial temperature data close to the burner surface. The closest distance to the burner surface is equal to the radius of the thermocouple bead. An alternative radiation correction procedure [33] was also used, assuming an emissivity value of 0.2 [34]. The results were found to be nearly identical to that of Shaddix [31].

Soot PSDFs were probed within the BSS flame configuration. The same design of sampling probe, along with the stagnation plate in which the sampling probe is imbedded, was used for all laboratories. An 8 cm diameter by 1.3 cm thick aluminum disc acts as the flow stagnation surface. Water cooling coils were attached to the top of the disc and a thin-wall, 0.635-cm stainless steel tubular sampling probe was embedded into the disc. The tube wall is flush with the bottom surface and parallel to the flat flame. The burner-to-probe separation distance, H_p, can be resolved to an accuracy of ±0.025 cm. The plate temperature was measured by a type-K thermocouple embedded within the disc. The flame sample was drawn into the probe through a laser-drilled orifice that ranges in diameter from 127 μm at Stanford to 160 μm at Tsinghua. The orifice was positioned on the center axis of the burner facing the incoming flame gas.

In each laboratory, the soot sample drawn into the probe was immediately diluted with a cold flow of nitrogen at 30 L/min (298 K & 1 atm). The flow rate into the orifice or the dilution ratio was controlled by fine pressure adjustment across the orifice. The pressure drop across the orifice, ΔP_o, was measured by a manometer upstream and a manometer downstream of the sampling orifice. At Stanford, the dilution ratio was determined as function of ΔP_o by two independent methods as shown in Table 2. In the first method, the mole fraction of CO_2 was determined by an NDIR analyzer in a stoichiometric C_2H_4-O_2-20% Ar-40% CO_2 flame. In the second method, a flow of air coming out of the tube through the orifice was measured by a Sensidyne Gilibrator-2 flowmeter at room temperature. Both methods require corrections for the difference in gas density and viscosity between calibration gas and the actual gas sample of the flame.

One of the quantities of interest is the absolute particle number density, N, in the flame, which is related to the number density measured by SMPS, N_s, through the dilution ratio, DR,

$$N = DR\, N_s\,. \tag{1}$$

The dilution based on CO_2 measurement was defined in terms of the measured CO_2 mole fraction, $x_{CO_2,m}$, and the predicted CO_2 mole fraction , $x_{CO_2,p}$, which was taken from solution of the underlying flame through 1-D stagnation flame modeling. Similar to previous studies, the flow through the orifice was assumed to be a fully developed laminar flow such that the flow rate is inversely proportional to the gas viscosity, μ [35, 36]. Thus, the dilution ratio may be determined as

$$DR = \left(\frac{x_{CO_2,p}}{x_{CO_2,m}}\right)\left(\frac{T_0}{T_s}\right)\left(\frac{\mu_{m,f}}{\mu_{m,c}}\right) \tag{2}$$

where T_0 is the temperature of the diluent, carrier gas in probe (T_0 = 298 K) and T_s is the temperature of the flame gas sample drawn into the orifice, which was assumed to be equal to the stagnation surface temperature, and $\mu_{m,f}$ and $\mu_{m,c}$ are the mixture viscosities of Flame C3 and the calibration flame with 20% Ar and 40% CO_2 as the diluent, respectively. Correction for viscosity amounts to 15% between the two flames.

The second method measures the flow rate of air out the orifice from the ambient air. For a given ΔP_o drop, the dilution ratio was measured by

$$DR = \left(\frac{L_s}{L_{air}}\right)\left(\frac{T_0}{T_s}\right)\left(\frac{\mu_{m,f}}{\mu_{air}}\right) \tag{3}$$

where L_s and L_{air} are the volumetric flow rates of dilute nitrogen gas and ambient air sample drawn into the orifice, respectively. Since the method does not use a flame, both L_s and L_{air} are at the room temperature. The viscosity correction results in 60% increase in DR as a result of higher viscosity of the argon-diluted flame gas relative to the cold air viscosity. The dilution ratio thus measured is plotted as a function of ΔP_o as shown in Fig. 1. The two independent methods produce very close dilution ratio values over the entire range of ΔP_o tested, giving the correlation

$$\log DR = 1.89 + \frac{0.28}{\log\left(0.0233\Delta P_o\right)}, \tag{4}$$

where ΔP_o is in mmH_2O. The uncertainty of eq 4 is estimated to be ± 40% as shown by the dashed line in Fig. 1, although the actual uncertainty is probably smaller than the above assignment. As will be discussed later, the 1-D stagnation simulation does not accurately describe the predicted CO_2 concentration for every dilution ratio, therefore, a portion of the above uncertainty can be attributed to this limitation. Only method 2 was used at Shanghai Jiao Tong and Tsinghua for the respective probes used.

The soot sample was analyzed by mobility sizing using TSI SMPS systems. At Stanford, a TSI model 3080 Electrostatic Classifier with a 3085 nano-Differential Mobility Analyzer (DMA) and Kr-85 Neutralizer was combined with a TSI 3025 ultrafine Condensation Particle Counter (CPC). The same Electrostatic Classifier and DMA were used at Shanghai Jiao Tong and Tsinghua but the particle counter is a more recent model (TSI 3776). Electrically conductive tubing was used to connect the sample probe to the SMPS, keeping the distance between the sampling orifice and the SMPS inlet as short as possible (about 50 cm in each laboratory).

During mobility measurements, the sample and sheath flows through the nano-DMA were 1.5 and 15 L/min, respectively. These flow rates allow for particles to be classified in the range of 2-64 nm. Limitations in the SMPS flow rate accuracy cause a 2% error in the mobility diameter. The sampling orifice eventually becomes clogged with soot over time so the SMPS scan time was 50 seconds up and 10 seconds down for each lab as a compromise between size distribution smearing at short times and orifice clogging at long scan times. In addition, the sampling orifice was cleaned after each scan with a fine needle. Mobility measurements can overestimate the physical size of particles smaller than 10 nm because of inherent limitations of the empirical Cunningham slip correction. Here, a parameterized correlation is applied to correct the mobility diameter as discussed in previous studies [3, 14-16].

The mass of nascent soot from Flame C3 was measured by a Cambustion Centrifugal Particle Mass Analyzer (CPMA) at UC Riverside on the Stanford burner setup. Aerosol particles with a known charge distribution are subjected to a rotational flow in the CPMA such that the particles are accelerated outward. An electric bias voltage is then applied which opposes the acceleration of the particles so that centrifugal and electrostatic forces can balance. Particles are thus classified by the particle mass-to-charge ratio without having to know particle shape or morphology. In the current study, the mass classification of the CPMA was calibrated using a polystyrene latex (PSL) aerosol of known diameter and density. Standard PSL particles 70 and 100 nm in diameter were nebulized with deionized water using an aerosol generator (model 3076, TSI) and dried in diffusion dryers. The mobility diameter and mass were subsequently measured. A systematic bias in mobility particle sizing was found due to 4% error in sheath air flow rate of the SMPS. A correction was made to the sheath flow rate for all subsequent data processing for accuracy. The error in determination of particle mass was found to be 6 and 5% for 70 and 100 nm PSL particles, respectively. This is in the range of uncertainties reported in earlier studies. For example, Symonds et al. [37] reported 6% for a DMA-CPMA system based on the uncertainty analysis. McMurry et al. [38] reported 5% uncertainty using a DMA-APM system.

A diagram summarizing the setup at UC Riverside for tandem mass and mobility measurements is shown in Fig. 2. The diluted flame sample was sent downstream for analysis at a flow rate of 1.5 L/min and the rest of the sample was sent to the exhaust. A known charge distribution was then applied to the soot sample by a X-ray particle neutralizer before being introduced into the CPMA. The rotational speed and voltage were then set in the CPMA to classify the polydisperse aerosol by a chosen mass. For each mass classification, the monodisperse aerosol with respect to mass was sent to the electrostatic classifier where the voltage was scanned (TSI model 3085 Nano-DMA, 10:1.5 sheath-to-sample flow, 50 sec up-scan, 10 sec down-scan) to measure the mobility diameters in the range of 2.5-79 nm. A mobility diameter distribution corresponding to each mass classification was then obtained by counting the particles in a TSI model 3776 CPC. Mobility diameter distributions were measured for CPMA classified masses ranging from 2 to 113 attograms.

3. Computational Methods

The experimental configuration was modeled at Stanford first as a pseudo 1-D stagnation flow flame [39, 40] using a modified version of OPPDIF [41]. Details of the simulation are available elsewhere [3]. Our objective was not to model soot formation. Instead the model is used to explore the flame conditions, assess the accuracy of the temperature measurement and assess the impact of the boundary conditions. The cold boundary temperature is the extrapolated gas temperature measured close to the burner surface. The flow is a uniform plug flow with a mass flux given by the experimental cold flow velocity and reactant composition. The species mass flux is determined by the balance of the convective and diffusive velocities. The stagnation surface, located at $x = H_p$, is treated as a non-slip wall. The axial, radial and diffusive velocities are all zero. It has a temperature, T_s, equal to the measured plate temperature. The net diffusive velocity was assumed to vanish at $x = H_p$. However, in the absence of a finite flow through the sampling orifice, the significant temperature gradient at or near $x = H_p$ drives Soret diffusion which is counterbalanced by Fickian diffusion.

The OPPDIF solution was calculated using windward differencing, multicomponent transport and thermal diffusion. Heat release rates and transport properties were calculated using Sandia CHEMKIN [42] and TRANFIT [43]. Radiative heat loss by CO_2 and H_2O was considered in these simulations. The reaction kinetic model used was USC Mech II [44], which includes the production of benzene and toluene but does not include PAH or soot chemistry. Adaptive mesh resolution was used and it was found that the flame is sufficiently resolved with roughly 200 grid points.

The aforementioned pseudo 1-D simulation was repeated at Duisburg using Cantera [45]. Compared to the OPPDIF calculation, the two simulations differ in the following aspects. While the OPPDIF calculation used multicomponent transport along with thermal diffusion, the Cantera calculation used mixture-average formula without thermal diffusion. One additional difference is that the OPPDIF calculation considered radiative heat loss from CO_2 and H_2O, whereas the Cantera calculation did not.

The governing equations and solution method for 2-D axisymmetric simulations have been discussed earlier [46]. Briefly, the simulation software is based on OpenFOAM [47] in a finite volume framework for continuum mechanics allowing for implementation of finite-rate reaction kinetics. The software was supplemented by a detailed model of diffusive transport. The formula of Wilke [48] was used to calculate the dynamic viscosity of the mixture, while the equation of Mathur and Saxena [49] was used for calculation of the mixture heat conductivity. The pure species transport properties were calculated for a broad range of temperatures using Cantera prior to a 2-D simulation. The molecular diffusivity was approximated using the mixture-averaged formulation [50]. The convective transport of the scalar quantities was discretized using a total variation diminishing scheme of second-order accuracy, while the momentum, the diffusive terms and the pressure gradient were discretized using central differencing. Again, our focus is the flame condition and flow field, and as such soot formation was not considered, neither was the radiative heat loss from the flame gas or soot in the 2-D calculation. The 2-D simulations were carried out for cases with a closed orifice and an open orifice on the centerline of the stagnation surface. The simulation was carried out for H_p = 0.55, 0.6, 0.7, 0.8, and 1.0 cm with the boundary conditions taken from the experiment. The 2-D simulations exclusively used the 32-species reaction model of Luo et al. [51] which is a skeletal model of ethylene combustion derived from USC Mech II [44].

The integration chosen for the 2-D simulation was a rectangular, axisymmetric projection of the burner including the co-flow region. The grid resolution was variable (non-uniform), the orifice with a radius of 75 μm was resolved by 10 cells and the total number of cells on the orthogonal grid was 56,200 for the case of H_p = 10 mm. The solution convergence was tested by coarsening of the grid up to a resolution of 12,300 cells and to a resolution of 5 cells across the orifice radius. At the inflow boundary, fixed velocities, temperatures and mass fractions of unburned gases were imposed. Treatment of inlet diffusion and implementation of the transport models was described in detail by Deng et al. [46]. The flow field quantities at the burner outlet boundary were extrapolated from the solution inside the domain, while any flow back into the domain was suppressed. The orifice was treated as an outflow boundary. Both the convective and the diffusive fluxes were calculated by linear interpolation resulting in a central differencing scheme.

4. Results and Discussion

Facility effects and Experimental Sensitivity Analyses

A comparable technique for measuring the local gas-phase temperature in the flame is established first so that the observed kinetic processes of soot formation are well characterized. The comparison among the measured axial flame temperature is shown in Fig. 3 using H_p = 1.0 cm as an example. The data shown are corrected for radiation. The work here shows that the axial temperature profile is not influenced by burner size or type. The data reported by Abid et al. [3], who used the 7.6 cm burner (see Table 1), are also shown for comparison. The agreement between the three facilities is excellent. The peak temperature measured is within 20 K of each other. The post-flame region of the temperature profile shows slightly more variations with the Tsinghua measurements being lower than the rest. A primary source for positional uncertainty and discrepancies in the pre-heat and post-flame region is the different tension applied to the fine-wire thermocouple.

Abid et al. [3] solved the detailed flame structures using experimentally measured temperature boundary conditions. The computed temperature profile as reported in [3] are shown in Fig. 3. Also shown in the figure are the profiles computed at Duisurg, comparing results obtained using 1-D Cantera with USC Mech II, 1-D Cantera with the reduced model of 32-species, and 2-D OpenFOAM simulation without the orifice flow. The agreement is satisfactory between experiment and model prediction. The largest discrepancy occurs in the post-flame region and this may be caused by changes in thermocouple emissivity resulting from soot deposition onto the surface. Another source of positional uncertainty is from to the finite elasticity and thermal expansion of the thermocouple wire. The flow exerts a drag on the wire and this drag decreases significantly close to the stagnation surface. The four computational cases shown are in good agreement with each other. The slightly higher temperature in the flame region from the 1-D Cantera calculation as compared to the OPPDIF results may be attributed to radiation by H_2O and CO_2 not accounted for in the Cantera calculation. Most notably, the 1-D results are all in good agreement with the 2-D results, indicating that the flow field of the flame studied can be accounted for by the stagnation flow formulation [39].

Axial temperature measured in the 5.0 cm burner at Stanford is shown in Fig. 4 for burner-to-stagnation surface separations ranging from H_p = 0.4 to 2.0 cm. The vertical error bars of Fig. 4 represent the uncertainty in the emissivity of the thermocouple coating (0.3–0.6). This is by far the greatest uncertainty among all factors considered. The horizontal error bars indicate positioning inaccuracy. The computed temperatures generally fall within the error bars for all H_p values tested. This experiment-model agreement is encouraging in that the flame structure can be calculated with relative ease, and that experiment and model may now be compared directly without invoking an arbitrary spatial shift.

Particle sampling can be impacted by two sources of inaccuracy, both resulting from particle losses [35], both of which may be minimized if appropriate sample dilution ratios are chosen. It can be shown that when optimized, the PSDF is insensitive to the dilution ratio and should stay insensitive over a fairly wide range of the dilution ratio. Relevant examples are illustrated in Fig. 5. For high dilution ratios, e.g., DR = 1331 as shown, the velocity of the soot sample passing through the orifice is low and this leaves ample time for small particles to diffuse to the orifice wall. Under this condition, most of the small particles would be lost (the open triangles of Fig. 5). In contrast, for low dilution ratios the high particle number density in the sampling line promotes particle-particle coagulation, leading to a reduced total number density and larger particle size (the open circles of Fig. 5). These loss mechanisms are minimized in the middle range of dilution where the PSDFs are seen to be insensitive to the dilution ratio. The above principle can be demonstrated more clearly by examining the variation of total particle number density and median mobility diameter $<D_m>$ as a function of the dilution ratio, as shown in Fig. 6. It can be seen that both N and $<D_m>$ are insensitive to the dilution ratio in the appropriate range of dilution. In contrast, $<D_m>$ increases and N decreases outside this range of dilution.

We now shift to facility effects on the PSDF measurement. The measured PSDF for all facilities are reported in Fig. 7. The burst of nucleation sized particles was observed in all facilities at H_p = 0.40 cm and a drastic increase in the number of nucleation size particles (D_m < 5 nm) is observed at H_p = 0.45 cm. As the burner-to-stagnation surface separation increases a shoulder appears in the PSDF. At H_p = 0.70 cm, the PSDF develops into a distinct bimodal distribution which indicates persistent nucleation combined with mass/size growth. At larger burner-to-stagnation separations, soot nucleation is less prominent and the PSDF transitions to a unimodal distribution in the range of particle size observed.

The facility dependence is small, as shown in Fig. 7. The PSDFs are also insensitive to burner size, as expected. The PSDFs obtained from each facility overlap each other throughout the range of H_p observed. The largest discrepancy occurs at lower burner-to-stagnation surface separations as observed at H_p = 0.40 cm and for the PSDF shape observed at H_p = 0.55 cm. The burst in nucleation and rapid transition to a shouldered PSDF occur within the 0.2 cm distance thus making the observed PSDFs highly sensitive to positional accuracy. The evolution of the PSDFs is slower towards the later growth stage (H_p > 1.0 cm) and the measured PSDF is not as sensitive to the position uncertainty.

To illustrate the large sensitivity of measured PSDFs to positional accuracy, the PSDF measured at H_p = 0.49 cm, shown in Fig. 8, is plotted along with those resulting from offsetting the position by ±0.02 cm. Clearly, small positional inaccuracy in the nucleation region can lead to large changes in the PSDF. In contrast, the sensitivity of the measured PSDF to other operating parameters was found to be small, at least away from the nucleation region. For example, Fig. 9 shows four sets of PSDF data collected for T_s ranging from 385 to 500K. The PSDF shape and the total number density are completely insensitive to T_s. This result is certainly interesting since our expectation is that the stagnation surface temperature should exert an impact, albeit a small one on the PSDF, if the transport of the particle sample into the orifice is driven by thermophoresis. The lack of sensitivity to the stagnation surface temperature suggests that the convective flow in front of the probe orifice is at play, an issue to be discussed in more detail later. The sensitivity of the measured

PSDF to the shroud N_2 velocity is shown in Fig. 10 for velocity between 10 and 44 cm/s. The PSDF are found again to be insensitive to this variation.

Integration of the detailed PSDF with respect to mobility diameter yields the total number density, N. In addition, the soot volume fraction F_v was derived from the PSDF by assuming all particles are spherical with diameter equal to the mobility diameter. As will be discussed later, the particles probed are not spherical and the volume fraction data shown here are only for the purpose of comparing data collected from the different facilities. Caution should be exercised when the volume fraction data are used for model comparison. As one would expect, the good agreement in the PSDFs across the 3 facilities carries over to these global sooting properties, as seen in Fig. 11. The error bars for each data point amount to ±40%, due to dilution uncertainty and ±0.025 cm due to positional uncertainty. The 95% confidence interval was determined for the volume fraction and number density by considering all four sets of the data obtained in the current study. These are shown in the same figure by the thick error bars. As discussed earlier, the largest PSDF variation in experimental observation across the facilities is during the nucleation and early growth stages, where the confidence intervals are correspondingly large.

Interestingly, earlier measurement on the same benchmark flame [3] yielded different results especially in the early stage of the soot formation process. As compared in Fig. 11, the nucleation burst occurs substantially later in the data report by Abid et al. [3]. The spatial offset is roughly 0.15 cm. The final volume fraction and number density are however the same in both studies. This discrepancy clearly deserves an explanation especially in light of the agreement across the current facilities and the fact that the current Stanford measurements also used the same 7.6-cm burner used in Abid et al.

After a concerted study that eliminated many possible causes, one explanation stands out. That is, the porous plug of the burner must have changed its pore density distribution after a lengthy use during the period of experiments of [3]. To illustrate this problem, we first plot in Fig. 12 the radial temperature distributions determined at a distance of 0.18 cm from the burner surface with H_p = 1.0 cm. The left panel of the plot examines the potential impact of the stagnation surface on the radial temperature profile for the 5.0 cm burner. It is seen that the temperature stays constant until it reaches the edge of the flame, as expected, and that the stagnation surface does not impact the temperature in the radial direction. The right panel shows that the 7.6-cm burner exhibits the same behavior and that the two burners generated flames of temperature that are within 10 K of each other. Suffice to note that the measurements shown were made when the porous plugs in both burners were relatively fresh, and the radial temperature variation seen in Fig. 12 is an indicator that the burner operated properly.

Two problems can occur when the burner is not operated properly and/or the porous plug is aged due to repeated use. Neither can be detected visually and the problem is best detected by examining the radial temperature distribution in the main flame zone as shown in Fig. 13. A loose fitting porous plug causes the unburned gas to flow preferentially along the plug rim. This creates a non-uniform distribution of enthalpy rate and a lower temperature along the center of the flame relative to the edge. As shown in the same figure, the problem is removed when a tight seal is achieved with Teflon tape wrapped around the circumference of the porous plug.

The second problem is more difficult to detect, but it yields the same result as a loosely fit porous plug: as the porous plug ages the repeated heating and cooling causes the pores in the center of the plug to contract and the outer edge to expand. The smaller pore sizes of the plug center produce a smaller local flow rate and thus enthalpy injection rate, which again leads to a lower temperature along the centerline of the flame and a higher temperature towards the flame edge, as shown in Fig. 13. The centerline temperature measured by Abid et al. is nearly identical to those of the current study (Fig. 3). The probe sampling/SMPS analysis of that study was done after the temperature measurement was complete. Therefore, either the porous plug was aged or it was not properly mounted when Abid et al. carried out the SMPS experiment. The lower centerline temperature that resulted caused the soot to nucleate later in the flame and produced the differences in the F_v and N profiles observed in Fig. 11. A previous report on the same premixed ethylene flame at several flame temperatures [30] showed the final volume fraction reaches a broad peak as a function of temperature at these conditions; hence the current sensitivity of the final F_v to the centerline temperature is weak. The uniformity of the radial temperature should be checked routinely to ensure the flame is actually flat and the aforementioned issues are avoided. Presently, it is unclear whether the porous plug in the McKenna burner exhibits the same aging behavior.

Mobility Mass versus Actual Mass

Particle mass was measured in tandem with the mobility diameter. Nascent soot was classified by mass in the CPMA, producing a mono-mass aerosol that was subsequently analyzed for the mobility diameter distribution. This is a configuration similar to APM-SMPS adopted by Malloy et al. [52] for real-time density measurement. An aerosol mass classifier followed by a mobility classifier has advantages of shorter scanning time and higher mobility resolution. A series of PSDFs corresponding to the classified mass is shown in Figures S1 and S2 for H_p = 0.8 and 1.2 cm, respectively of the Supplemental Materials. For each mono-mass aerosol the geometric standard deviation of the mobility diameter is in the range of 1.06 to 1.08 assuming a lognormal distribution. The non-unity geometric standard deviation is consistent with mass broadening of around 10% in the CPMA. Therefore, the data also suggest that the morphological variation leading to mobility diameter variation is relatively small for a given particle mass.

The relationship between the mobility diameter and particle mass measured for the two burner-to-stagnation surface separations, H_p = 0.8 and 1.2 cm is shown in Fig. 14. A family of curves is also drawn to show the relationships for spherical particles using mass density values of ρ_s = 1.5, 0.8 and 0.7 g/cm^3. An inspection of the plot shows that a spherical particle model cannot explain the observed D_m-versus-m relationship if the mass density value of 1.5 g/cm^3 is used [53]. For comparison, the 96th edition of the CRC Handoook gives mass density values of 1.27 and 1.37 g/cm^3 for pure pyrene and coronene, respectively, at room temperature. The inset of Fig. 14 shows that the mobility spherical mass ($m_m = \rho_s \pi D_m^3/6$), calculated by assuming a spherical particle shape with ρ_s = 1.5 g/cm^3, is larger than the actual particle mass, m, by about a factor of 2 to 3. Hence, the spherical-particle assumption alone could yield errors of a factor of $2^{1/3}$ to $3^{1/3}$ in model and experimental PSDF comparison.

In fact, the data collected support an effective mass density of 0.7 to 0.8 g/cm^3. This indicates that the non-spherical morphology impacts the mobility diameter. Hence, the observed D_m-versus-m relationship is indicative, to an extent, of the particle morphology. The ratio of the mass obtained by taking the spherical assumption to the actual mass (m_m/m) is plotted in Fig. 15. The symbols were derived from the D_m-versus-m data assuming ρ_s = 1.5 g/cm^3. Deviation of this mass ratio value from unity corresponds to the deviation from the spherical shape. For the two H_p values probed, the "older" particles (H_p = 1.2 cm) show greater deviations from the sphericity than the "younger" particles (H_p = 0.8 cm), as one would expect. Older particles are expected to exhibit greater fractal features than the younger ones.

The measured m_m/m values are superimposed with the ratio obtained by comparing the mass of four idealized shapes (ρ_s = 1.5 g/cm^3) to the actual mass measured. The shapes are listed below:

(1) a cylinder with spherical caps (or a prolate spheroid) of overall length L and diameter D (the dashed horizontal lines);

(2) a chain of n-spherical particles in point contact (the solid horizontal lines);

(3) ballistic particle-cluster aggregates (BPCA, the slanted solid lines);

(4) diffusion-limited particle-cluster aggregates (DLA, the slanted dashed lines).

The mobility diameter may be determined for models 1 and 2 using expressions of the drag force in the rigid body limit [54] averaged over orientations following Chan and Dahneke [55]. The prolate spheroidal model has been used in earlier kinetic studies of nascent soot oxidation [56]. The aggregate morphology can vary depending on the dominant mode of transport of the primary particles. In BPCA aggregates, the convective velocity dominates the motion and diffusion dominates in DLA aggregates. Large carbon aggregates, i.e., those that can be described by models 3 and 4, have been shown to follow a scaling law where the number of primary particles, n_p, increases with aggregate cross section, A_a [57, 58]:

$$n_p = k_a \left[\frac{A_a}{A_p} \right]^{D_a} \qquad (5),$$

where k_a is a constant, A_p is the cross-section of the primary particle and D_a is the exponent which characterizes the scaling. In the free molecule regime, the mobility diameter, D_m, is a measure of the collision cross-section and thus it is related to the total particle cross-section [58] as

$$D_m = \left(\frac{4}{\pi} A_a \right)^{1/2} . \tag{6}$$

The values of K_a and D_a may be taken from Eggersdorfer and Pratsinis [59] for the two morphological models accordingly, assuming that the geometric standard deviation of the primary particle size distribution is 1.44 [36].

It may be seen from Fig. 15 that the morphology of the particles at H_p = 0.8 cm can be explained satisfactorily by a ρ_s value of 1.5 g/cm^3 with either a 4-sphere chain model or by the DLA and BPCA models with primary particle size around 10 nm or smaller. In the small size end, the morphology of particles sampled at H_p = 1.2 cm are consistent with 4-sphere model, and with the BPCA or DLA models having primary particles sizes between 5 to 20 nm. The finding of the current study supports and, to an extent, further quantifies the results of microscopy analyses of Schenk et al. [17-19]: even at an early stage of growth, nascent soot deviates from sphericity at almost all sizes.

Probe Effects and Two-Dimensional Flow Field

Flame gas sampling requires a finite flow rate through the sampling orifice. The stagnation point along the centerline of the flame is therefore not stagnant. At a dilution ratio of 500 and 30 L/min of cold diluting flow as discussed before, the gas linear velocity exceeds 50 m/s in the orifice. Hence, the soot sample taken should be an average of some volume in front of the orifice because the local flow and temperature is perturbed by the sampling flow. The 1-D simulation currently applied cannot capture the full flow field immediately upstream of the sample orifice.

To assess the aforementioned probe effect, we carried out 2-D axisymmetric simulations with and without a sample orifice. Without the orifice, 2-D simulations yield centerline temperature profiles in close agreement with experiment and 1-D simulation results for all five H_p values simulated (see, Figure S3 of the Supplemental Materials). The temperature in the flame and post-flame region is only slightly higher than the 1-D results because the radiation by CO_2 and H_2O was not considered in the 2-D simulation. With the orifice open at a pressure drop of 0.01 bar (a dilution ratio of ~400), the non-zero velocity through the sampling orifice now gives rise to several features that are important to the discussion of the probe effect.

A comparison of 1-D and 2-D models for flame temperature and axial velocity highlighting the effect of the finite flow during probe sampling is shown in Fig. 16. The orifice flow has a small, though not negligible effect on the flame. As Fig. 16 shows, the temperature at the centerline "stagnation" point is substantially higher than the true stagnation point temperature, obviously due to the finite convective flow at that point. Also along the centerline, the axial velocity takes a drastic upturn due to the sample flow. Under this condition, the stagnation point is no longer a "point" located in the center, but it forms a circular line around the inlet of the sampling orifice. Strictly speaking, the flow into the orifice cannot be modeled as a "flow into a stagnation point." Rather it should be a stream-tube with varying cross-section area being constricted up to the diameter of the orifice. The zone of this constriction of the stream-tube, where the gas is strongly accelerated, corresponds roughly to a half-spherical volume 0.2 cm in radius.

It is within this effective volume that the soot sample is drawn. The comparison between the convective flow time of the 1-D stagnation flow calculation and the centerline of the 2-D simulation with the orifice flow is shown in Fig. 17. For the current simulation condition, the time of the flame sample passing through the sampling volume is of the order of 1 ms. A different dilution ratio would introduce a different flow rate, and thus a different, effective sampling volume size and the sample residence time inside this volume. The fact that there exists a range of dilution ratios within which the PSDF is insensitive to the dilution ratio (Fig. 6) suggests that the sample taken is quite insensitive to the residence time and size of this effective sampling volume. This may be because surface reactions or coagulation are too slow to impact the PSDFs in the instant that the sample approaches the sampling orifice. Obviously, further investigation is needed in order to develop a proper one-dimensional model for this type of experiment. For now, we recommend that experimental PSDFs that are modeled using a 1-D stagnation flow model take into account the finite convective velocity due to sample flow by considering two limiting cases of computed PSDFs. In the sampling positions studied by 2-D simulation, the flow field was perturbed such that the PSDF "sample" has a contribution from soot that is 0.2 cm ahead of the stagnation point. This position may be considered to be the upstream limit for comparison between experimental data and modeling results.

5. Conclusions

The BSS flame configuration and related mobility PSDF measurement by probe sampling are studied in detail using four different burners of different sizes and makers in three separate facilities on the same benchmark ethylene-oxygen-argon flame. Furthermore, the relationship between the mobility diameter and particle mass was obtained for nascent soot using a tandem configuration consisting of a centrifugal particle mass analyzer followed by mobility size analysis. Detailed, 2-D axisymmetric numerical simulations were carried out focusing on the effect of finite sample probe flow rate on the boundary conditions of the flame and to understand the nature of the soot sample taken from the flame for subsequent analysis. The following conclusions are reached:

(1) Determination of nascent soot mobility PSDFs by probe sampling in BSS flames can be made more reproducible by placing tight control on the experimental flame boundary conditions and by careful sample dilution ratio calibration. A detailed procedure of dilution ratio determination is introduced for two independent calibration methods.

(2) Data generated from different burner sizes and makers over different research facilities are in agreement with each other within the experimental uncertainty of each facility. Data accuracy and appropriate comparison is best achieved with two separate measurable quantities. Here, we demonstrate that for the flame studied the facility effect is shown to be negligible in measurements of both the temperature profile and the mobility PSDF.

(3) Within the framework of the BSS flame/probe sampling technique, the sensitivity to the operating parameters, including the burner size, sheath flow rate, and stagnation surface temperature is insignificant. The greater sensitivity and uncertainty is related to the accuracy of

the burner-to-stagnation surface separation especially for small sampling positions corresponding to soot nucleation.

(4) The onset of soot nucleation reported by Abid et al. [3] for the same flame (Flame C3) is about 0.2 cm further from the burner surface than the current results. The cause for the discrepancy was attributed to aging of the burner porous plug plate during the experimental study of Abid et al., leading to closure of the pores around the center of the plate and thus a lower, local linear velocity along the centerline of the flame than expected. A method for routine inspection of the potential blockage of flow is suggested and demonstrated.

(5) Tandem particle mass and mobility analysis indicates that comparison of the experimental mobility size distribution with simulated particle size distribution by detailed modeling should be treated with some special care. In particular, treating particles of mobility diameter as small as 15 nm as spherical particles can lead to a factor of 2 to 3 error in particle mass. Nascent soot particles are found to deviate from sphericity even at the early stage of growth, in agreement with the earlier, microscopy observations. A proper comparison between the experimental mobility sizes and computed particle sizes should use the cross section area of the particles if simulations treat the aggregate nature of the particle. If the simulation assumes particle sphericity, the conversion of mass to mobility diameter should use an effective mass density of 0.7-0.8 g/cm^3. The current analysis supports the use of a mass density value of 1.5 g/cm^3 in computation of nascent soot size and mass growth.

(6) The probe sampling technique advanced in this and earlier studies still suffers from several non-idealities that will require further study. As revealed from detailed 2-D axisymmetric simulations that consider the micro flow into the orifice, the flow stagnation point of the BSS flame is not quite stagnant. The orifice flow creates a departure from 1-D stagnation flow approximation and this departure can be described, for the conditions studied, by a 0.2 cm radius half sphere in front of the orifice in which the flow accelerates as the gas sample is drawn into the orifice. The size of impacted volume is small enough such that it does affect the flame, but the soot sample analyzed should be an average of the flame gas in that finite volume. In absence of further

insight for the variation of the finite volume, we suggest to use PSDFs calculated at a distance of 0.2 cm from the stagnation surface for comparison with experimental PSDFs collected at the stagnation surface.

Acknowledgement

Work at Stanford was supported by the Combustion Energy, Frontier Research Center (CEFRC), an Energy Frontier Research, Center funded by the U.S. Department of Energy, Office of Science, Office of Basic Energy Sciences under Award Number DESC0001198. The authors from Shanghai Jiao Tong University acknowledge the Projects of International Cooperation and Exchanges National Natural Science Foundation of China (No. 51210010 and No. 91441129). The authors from Tsinghua University were supported by the National Basic Research Program (2013CB228502). The work at UC Davis was supported by the NSF under award number CBET1233038, and that at Duisburg was supported by the state of North Rhine-Westphalia. Dr. Saggese acknowledges the support from Politecnico di Milano for an extended exchange state at Stanford.

References

1. A. D'Anna, Proc. Combust. Inst. 32 (2009) 593-613.
2. H. Wang, Proc. Combust. Inst. 33 (2011) 41-67.
3. A. D. Abid, J. Camacho, D. A. Sheen, H. Wang, Combust. Flame 156 (2009) 1862-1870.
4. A. D. Abid, J. Camacho, D. A. Sheen, H. Wang, Energy Fuel. 23 (2009) 4286-4294.
5. J. Camacho, S. Lieb, H. Wang, Proc. Combust. Inst. 34 (2013) 1853-1860.
6. K. V. Puduppakkam, A. U. Modak, C. V. Naik, J. Camacho, H. Wang, and E. Meeks, A Soot Chemistry Model That Captures Fuel Effects, in: ASME Turbo Expo 2014: Turbine Technical Conference and Exposition, Düsseldorf, Germany, June 2014.
7. A. Abid, E. Tolmachoff, D. Phares, H. Wang, Y. Liu, A. Laskin, Proc. Combust. Inst. 32 (2009) 681-688.
8. R. P. Lindstedt, B. B. O. Waldheim, Proc. Combust. Inst. 34 (2013) 1861-1868.
9. A. Veshkini, N. Eaves, S. Dworkin, M. Thomson, Effect of Nucleation Reversibility on Predicting Soot Particle Size Distributions in Premixed Flames, in: 8th International Seminar on Flame Structure, Berlin, Germany, September 2014.
10. E. K. Y. Yapp, D. Chen, J. Akroyd, S. Mosbach, J. Camacho, M. Kraft, H. Wang, Combust. Flame 162 (2015) 2569-2581.
11. C. Saggese, S. Ferrario, J. Camacho, A. Cuoci, A. Frassoldati, E. Ranzi, H. Wang, T. Faravelli, Combust. Flame In Press.
12. C. K. Law, F. Wu, F. N. Egolfopoulos, V. Gururajan, H. Wang, Combustion Science and Technology 187 (2014) 27-36.
13. F. N. Egolfopoulos, N. Hansen, Y. Ju, K. Kohse-Hoinghaus, C. K. Law, F. Qi, Prog. Energy Combust. Sci. 43 (2014) 36-67.
14. Z. G. Li, H. Wang, Phys. Rev. E. 68 (2003) 061206.
15. Z. G. Li, H. Wang, Phys. Rev. E. 68 (2003) 061207.
16. Z. G. Li, H. Wang, J. Aerosol. Sci. 37 (2006) 111-114.
17. M. Schenk, S. Lieb, H. Vieker, A. Beyer, A. Gölzhäuser, H. Wang, K. Kohse-Höinghaus, ChemPhysChem 14 (2013) 3248-3254.
18. M. Schenk, S. Lieb, H. Vieker, A. Beyer, A. Gölzhäuser, H. Wang, K. Kohse-Höinghaus, Proc. Combust. Inst. 35 (2015) 1879-1886.

19. M. Schenk, N. Hansen, H. Vieker, A. Beyer, A. Gölzhäuser, K. Kohse-Höinghaus, Proc. Combust. Inst. 35 (2015) 1761-1769.

20. P. Mitchell, M. Frenklach, Proc. Combust. Inst. 27 (1998) 1507-1514.

21. P. Mitchell, M. Frenklach, Phys. Rev. E. 67 (2003) 061407.

22. B. Zhao, Z. W. Yang, Z. G. Li, M. V. Johnston, H. Wang, Proc. Combust. Inst. 30 (2005) 1441-1448.

23. J. P. Cain, J. Camacho, D. J. Phares, H. Wang, A. Laskin, Proc. Combust. Inst. 33 (2011) 533-540.

24. J. P. Cain, P. L. Gassman, H. Wang, A. Laskin, Phys. Chem. Chem. Phys. 12 (2010) 5206-5218.

25. J. S. Olfert, N. Collings, J. Aerosol. Sci. 36 (2005) 1338-1352.

26. K. Ehara, C. Hagwood, K. J. Coakley, J. Aerosol. Sci. 27 (1996) 217-234.

27. R. Ghazi, H. Tjong, A. Soewono, S. N. Rogak, J. S. Olfert, Aerosol Sci. Technol. 47 (2013) 395-405.

28. E. S. Cross, T. B. Onasch, A. Ahern, W. Wrobel, J. G. Slowik, J. Olfert, D. A. Lack, P. Massoli, C. D. Cappa, J. P. Schwarz, J. R. Spackman, D. W. Fahey, A. Sedlacek, A. Trimborn, J. T. Jayne, A. Freedman, L. R. Williams, N. L. Ng, C. Mazzoleni, M. Dubey, B. Brem, G. Kok, R. Subramanian, S. Freitag, A. Clarke, D. Thornhill, L. C. Marr, C. E. Kolb, D. R. Worsnop, P. Davidovits, Aerosol Sci. Technol. 44 (2013) 592-611.

29. D. C. Quiros, S. Hu, S. Hu, E. S. Lee, S. Sardar, X. Wang, J. S. Olfert, H. S. Jung, Y. Zhu, T. Huai, J. Aerosol. Sci. In press (2015).

30. A. D. Abid, N. Heinz, E. Tolmachoff, D. Phares, C. Campbell, H. Wang, Combust. Flame 154 (2008) 775-788.

31. C. R. Shaddix, Correcting Thermocouple Measurements for Radiation Loss: a Critical Review, in: Proceedings of the 33rd National Heat Transfer Conference, Albuquerque, NM, August 1999.

32. R. C. Peterson, N. M. Laurendeau, Combust. Flame 60 (1985) 279-284.

33. C. S. McEnally, U. O. Koylu, L. D. Pfefferle, D. E. Rosner, Combust. Flame 109 (1997) 701-720.

34. D. Bradley, A. G. Entwistle, Brit. J. Appl. Phys. 12 (1961) 708-711.

35. B. Zhao, Z. W. Yang, J. J. Wang, M. V. Johnston, H. Wang, Aerosol Sci. Technol. 37 (2003) 611-620.

36. B. Zhao, Z. W. Yang, M. V. Johnston, H. Wang, A. S. Wexler, M. Balthasar, M. Kraft, Combust. Flame 133 (2003) 173-188.

37. J. P. Symonds, K. S. J. Reavell, J. S. Olfert, Aerosol Sci. Technol. 47 (2013) 1-4.

38. P. H. McMurry, X. Wang, K. Park, K. Ehara, Aerosol Science & Technology 36 (2002) 227-238.

39. M. D. Smooke, I. K. Puri, K. Seshadri, Proc. Combust. Inst. 21 (1986) 1783-1792.

40. R. J. Kee, J. A. Miller, G. H. Evans, G. Dixon-Lewis, Proc. Combust. Inst. 22 (1989) 1479-1494.

41. A. E. Lutz, R. J. Kee, J. Grcar, F. M. Rupley, OPPDIF: A FORTRAN Program for Computing Opposed-Flow Diffusion Flames, Sandia Report 96-8243, Sandia National Laboratories, Albuquerque, NM, 1996.

42. R. J. Kee, F. M. Rupley, J. A. Miller, CHEMKIN-II: A FORTRAN Chemical Kinetics Package for the Analysis of Gas-Phase Chemical Kinetics, Sandia Report SAND89-8009, Sandia National Laboratories, Albequerque, NM, 1989.

43. R. J. Kee, G. Dixon-Lewis, J. Warnatz, M. E. Coltrin, J. A. Miller, A FORTRAN Computer Code Package for the Evaluation of Gas-Phase Viscosities, Conductivities, and Diffusion Coefficients, Sandia Report SAND86-8246, Sandia National Laboratories, Albequerque, NM, 1986.

44. H. Wang, X. You, A. V. Joshi, S. G. Davis, A. Laskin, F. N. Egolfopoulos, C. K. Law, USC Mech Version II. High-Temperature Combustion Reaction Model of H2/CO/C1-C4 Compounds., 2007,http://ignis.usc.edu/USC_Mech_II.htm.

45. D. Goodwin Cantera: An object-oriented software toolkit for chemical kinetics, thermodynamics, and transport processes. 2012, http://cantera.github.io/docs/sphinx/html/index.html.

46. L. Deng, A. Kempf, O. Hasemann, O. P. Korobeinichev, I. Wlokas, Combust. Flame 162 (2015) 1737-1747.

47. OpenCFD OpenCFD release OpenFOAM. 2012, http://www.openfoam.org/version2.1.0.

48. C. R. Wilke, J. Chem. Phys. 18 (1950) 517-519.

49. M. S. Mathur, S. C. Saxena, Appl. Sci. Res. 17 (1967) 155-168.

50. R. B. Bird, W. E. Stewart, E. N. Lightfoot, Transport Phenomena, John Wiley and Sons, 1960.
51. Z. Luo, C. S. Yoo, E. S. Richardson, J. H. Chen, C. K. Law, T. F. Lu, Combust. Flame 159 (2012) 265-274.
52. Q. G. Malloy, S. Nakao, L. Qi, R. Austin, C. Stothers, H. Hagino, D. R. Cocker III, Aerosol Sci. Technol. 43 (2009) 673-678.
53. B. Zhao, K. Uchikawa, H. Wang, Proc. Combust. Inst. 31 (2007) 851-860.
54. B. E. Dahneke, J. Aerosol. Sci. 4 (1973) 139-145.
55. P. Chan, B. Dahneke, J. Appl. Phys. 52 (1981) 3106-3110.
56. J. Camacho, Y. Tao, H. Wang, Proc. Combust. Inst. 35 (2015) 1887-1894.
57. A. I. Medalia, J. Colloid Interface Sci. 24 (1967) 393-404.
58. P. Meakin, Adv. Colloid Interface Sci. 28 (1987) 249-331.
59. M. L. Eggersdorfer, S. E. Pratsinis, Aerosol Sci. Technol. 46 (2011) 347-353.

Figure Captions

Figure 1. Viscosity-corrected dilution ratio determined at Stanford as a function of pressure drop across the orifice by two independent methods (symbols). The solid is a fit to data (Eq. 4); the dashed lines are the estimated uncertainty bounds.

Figure 2. Experimental setup for the tandem mass and mobility measurements of nascent soot particles at UC Riverside. CPMA – centrifugal particle mass analyzer; DMA – differential mobility analyzer; CPC – condensation particle counter.

Figure 3. Radiation-corrected, axial temperature profiles measured for H_p = 1.0 cm at each facility (symbols) compared to computed (lines) profiles. Computed temperature profiles are: 1-D OPPDIF simulation with USC Mech II as reported by Abid et al. (2009) [3], 1-D Cantera with USC Mech II, 1-D Cantera with the reduced model of 32-species, and 2-D OpenFOAM simulation using the reduced model without the orifice flow.

Figure 4. Experimental (symbols, Stanford 5.0-cm burner) and computed (lines, 1-D OPPDIF simulation using USC Mech II) axial temperature profiles for H_p where the detailed PSDF were measured. The experimental uncertainty shown represents the uncertainty in the emissivity of the coated thermocouple that ranges from 0.3 to 0.6 [3].

Figure 5. Selected mobility PSDFs measured at Stanford for H_p = 0.55 cm illustrating the impact of the dilution ratio employed on the size distribution measurement.

Figure 6. Effect of dilution ratio on the total number density and median mobility diameter of the PSDF measured at Stanford for H_p = 0.55 cm.

Figure 7. Mobility PSDFs measured at all facilities.

Figure 8. Sensitivity of the mobility PSDF to spatial position during the early soot growth stage. The measurement was done at Shanghai Jiao Tong.

Figure 9. Effect measured for the stagnation surface temperature on the mobility PSDF (top panel) and the median mobility diameter of the PSDF and number density (bottom panel). The measurement was done at Shanghai Jiao Tong.

Figure 10. Effect measured for the shroud velocity on the mobility PSDF (top panel), median mobility diameter and number density of the PSDF (bottom panel). The measurement was done at Shanghai Jiao Tong.

Figure 11. Volume fraction and number density measured at all facilities as a function of the burner-to-stagnation surface separation, H_p. Experimental uncertainty for each laboratory is shown by the thin, colored error bars and the confidence interval based on the scatter across the facilities and burner sizes is shown as heavy black bars.

Figure 12. Radial profile of the uncorrected temperature measured at a distance of 0.18 cm from the burner surface for the burner-to-stagnation separation H_p = 1.0 cm, comparing with or without the probe (stagnation surface) (left panel) and for two burner sizes (right panel). The temperature was not corrected for radiation heat loss. The measurement was done at Stanford University.

Figure 13. Radial profile of the uncorrected temperature measured at a distance of 0.18 cm from the burner surface for H_p = 1.0 cm, comparing an aged porous plug, a fresh but loose-fitting porous plug and the same fresh porous plug with edges sealed with Teflon tape. The temperature was not corrected for radiation heat loss. The measurement was done at Stanford University.

Figure 14. Relationship between the mobility diameter, D_m, and mass, m, measured for particles at two burner-to-stagnation separations (squares: H_p = 0.8 cm, circles: H_p = 1.2 cm), along with a family of curves for spherical particles of varying mass density values. Inset: the mass calculated from mobility diameter assuming sphericity and a mass density of 1.5 g/cm^3 for the particle material (mobility spherical mass, m_m) compared to the actual particle mass measured by CPMA.

Figure 15. Mobility spherical mass to actual mass ratio as a function of the actual mass, for an assumed mass density of ρ_s = 1.5 g/cm^3, comparing the measurements (symbols) and several models (lines) BPCA: ballistic particle-cluster aggregates; DLA: diffusion-limited particle-cluster aggregates; *n*-sphere: aggregates of *n*-primary spherical spheres; and $L/D = n$: cylinders with spherical caps of length, L, and diameter, D. The D_p value refers to the diameter of the primary particles in the aggregate. The banded areas indicate shapes that lie between a chain of spheres and a cylinder that are comparable on the basis of equal total lengths and primary particle or cylinder diameters.

Figure 16. Centerline temperature and axial velocity component computed for the case of H_p = 0.8 cm, comparing the results of 1-D stagnation flow calculation and of the centerline of the 2-D simulation with orifice flow.

Figure 17. Convective flow time computed for the case of H_p = 0.8 cm, comparing the results of 1-D stagnation flow calculation and of the centerline of the 2-D simulation with orifice flow.

Table 1. Key parameters of the experimental apparatus and models of Ultrafine Condensation Particle Counter (UCPC).

	Burner/porous plug						Sample orifice		Thermocouple		
Facility	Source	Body material	Plug material	Plug thickness (cm)	Pore size (µm)	Diameter (cm)	Diameter (µm)	Length (cm)	Wire diameter (µm)	Bead size (µm)	UCPC
Stanford	In-house	brass	bronze	1.3	10	5.0 & 7.6	127	30.5	130 [a]	300 [a]	3025
Shanghai Jiaotong	In-house	brass	bronze	1.3	10	5.0	130	30.5	150 [a]	380 [a]	3776
Tsinghua	McKenna	SS	bronze	1.5	70-130	6.0	160	30.5	135 [a]	320 [a]	3776

[a] Coated.

Table 2. Methods for calibrating the dilution ratio

Method	Flow Description	Quantity	Instrument	Probe temperature T_s (K)
1	CO_2 diluted flame	Mole fraction of CO_2	NDIR analyzer	500
2	Room air	Cold air flow rate	Flow meter	293

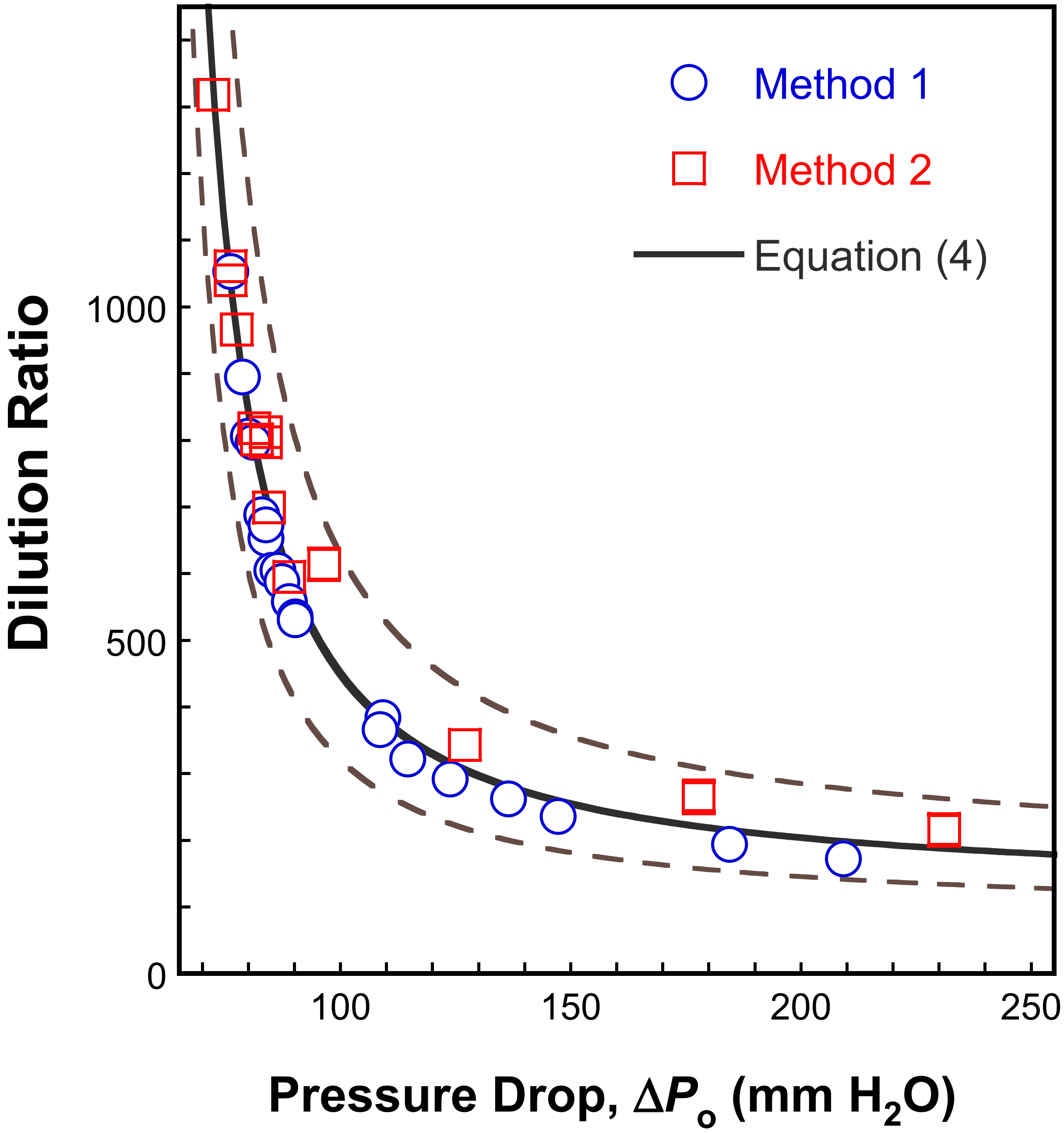

Figure 1. Viscosity-corrected dilution ratio determined at Stanford as a function of pressure drop across the orifice by two independent methods (symbols). The solid is a fit to data (Eq. 4); the dashed lines are the estimated uncertainty bounds.

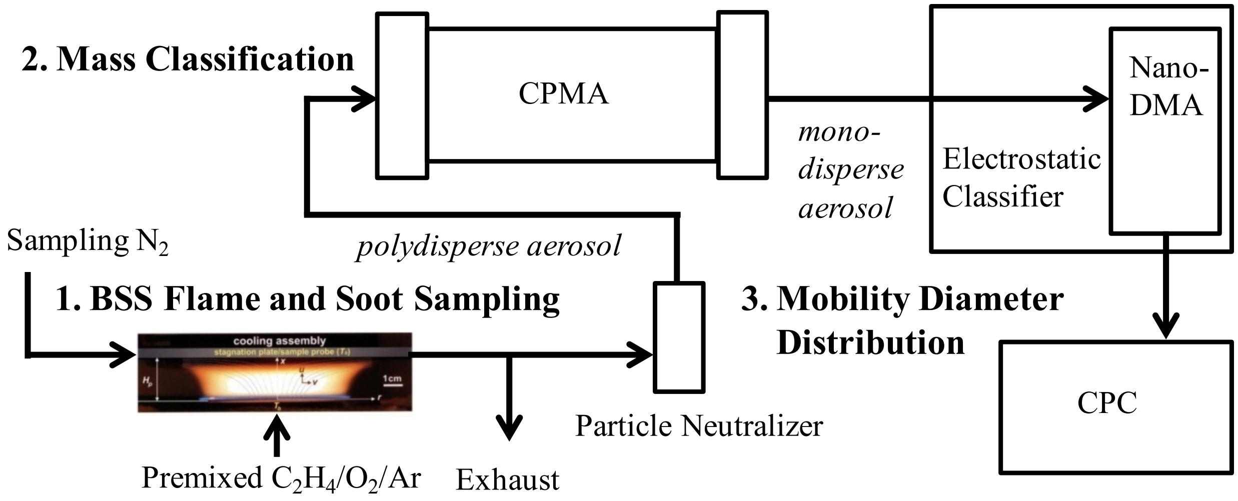

Figure 2. Experimental setup for the tandem mass and mobility measurements of nascent soot particles at UC Riverside. CPMA – centrifugal particle mass analyzer; DMA – differential mobility analyzer; CPC – condensation particle counter.

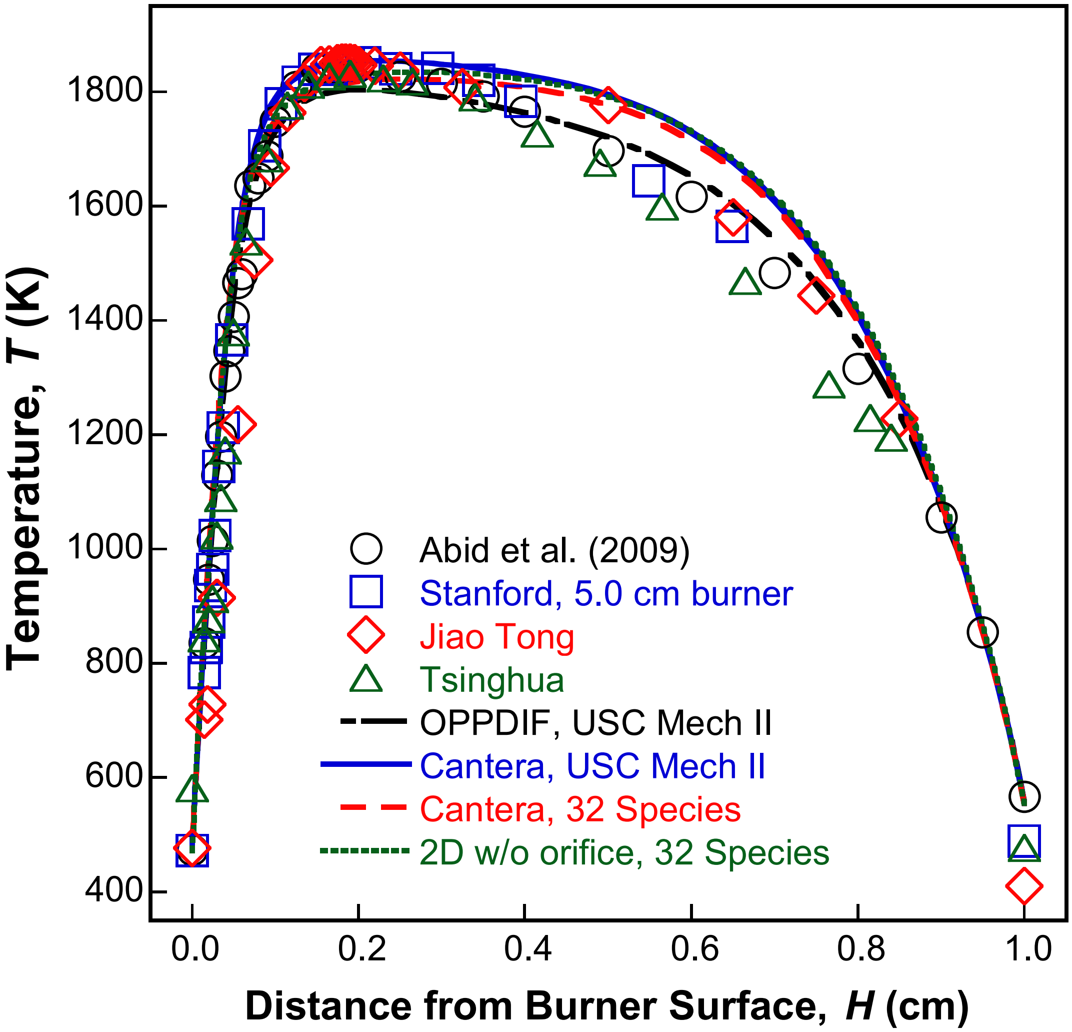

Figure 3. Radiation-corrected, axial temperature profiles measured for H_p = 1.0 cm at each facility (symbols) compared to computed (lines) profiles. Computed temperature profiles are: 1-D OPPDIF simulation with USC Mech II as reported by Abid et al. (2009) [3], 1-D Cantera with USC Mech II, 1-D Cantera with the reduced model of 32-species, and 2-D OpenFOAM simulation using the reduced model without the orifice flow.

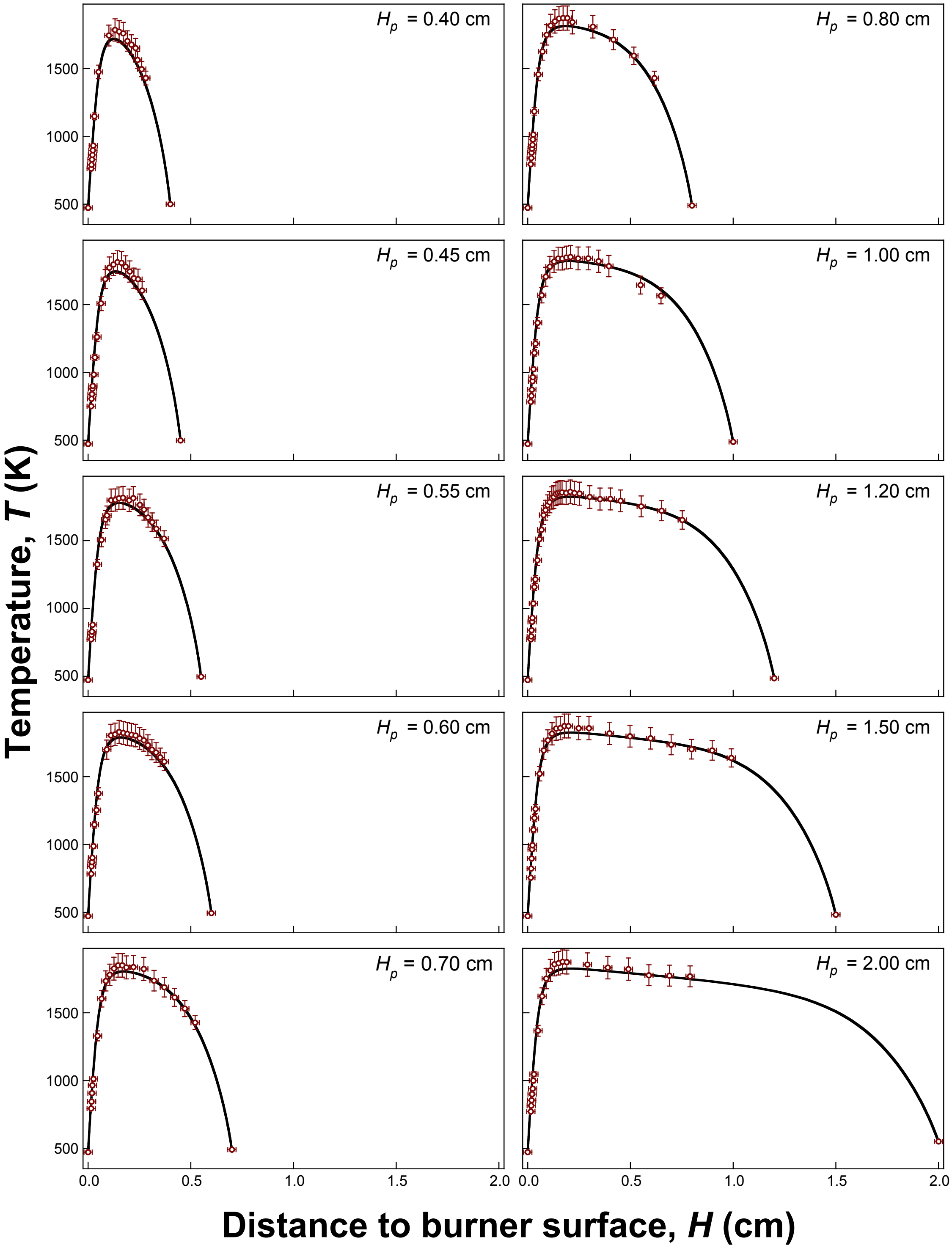

Figure 4. Experimental (symbols, Stanford 5.0 cm burner) and computed (lines, 1-D OPPDIF simulation using USC Mech II) axial temperature profiles for H_p where the detailed PSDF were measured. The experimental uncertainty shown represents the uncertainty in the emissivity of the coated thermocouple that ranges from 0.3 to 0.6 [3].

Figure 5

[Click here to download Figure: Figure 5.pdf]

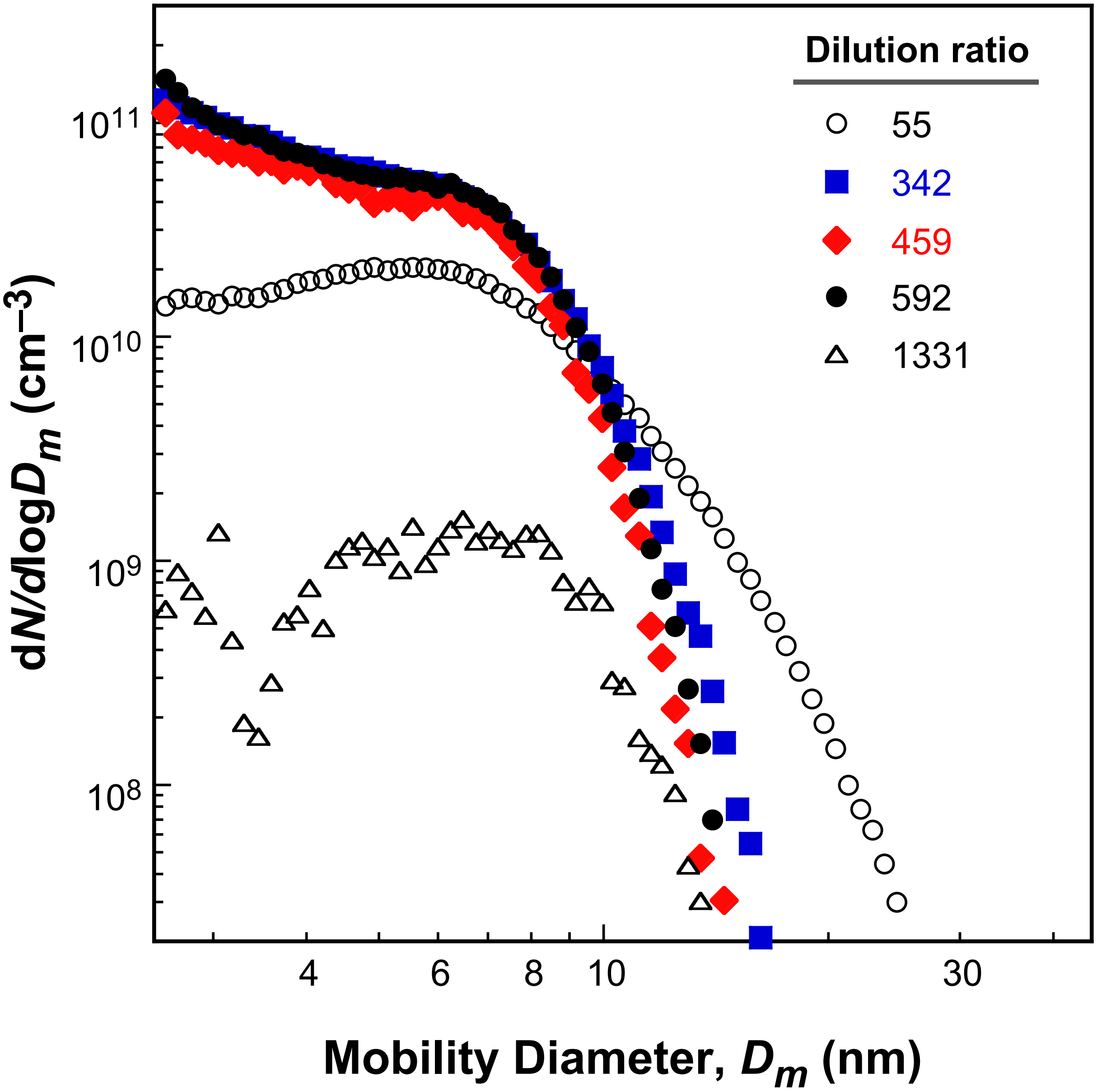

Figure 5. Selected mobility PSDFs measured at Stanford for H_p = 0.55 cm illustrating the impact of the dilution ratio employed on the size distribution measurement.

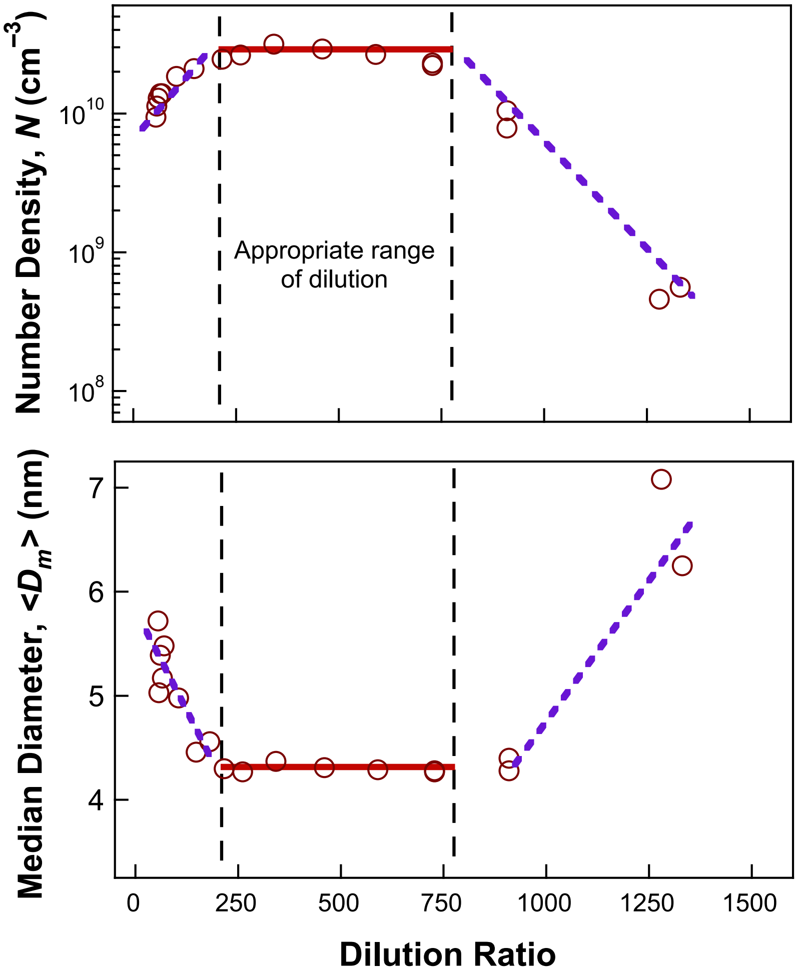

Figure 6. Effect of dilution ratio on the total number density and median mobility diameter of the PSDF measured at Stanford for $H_p = 0.55$ cm.

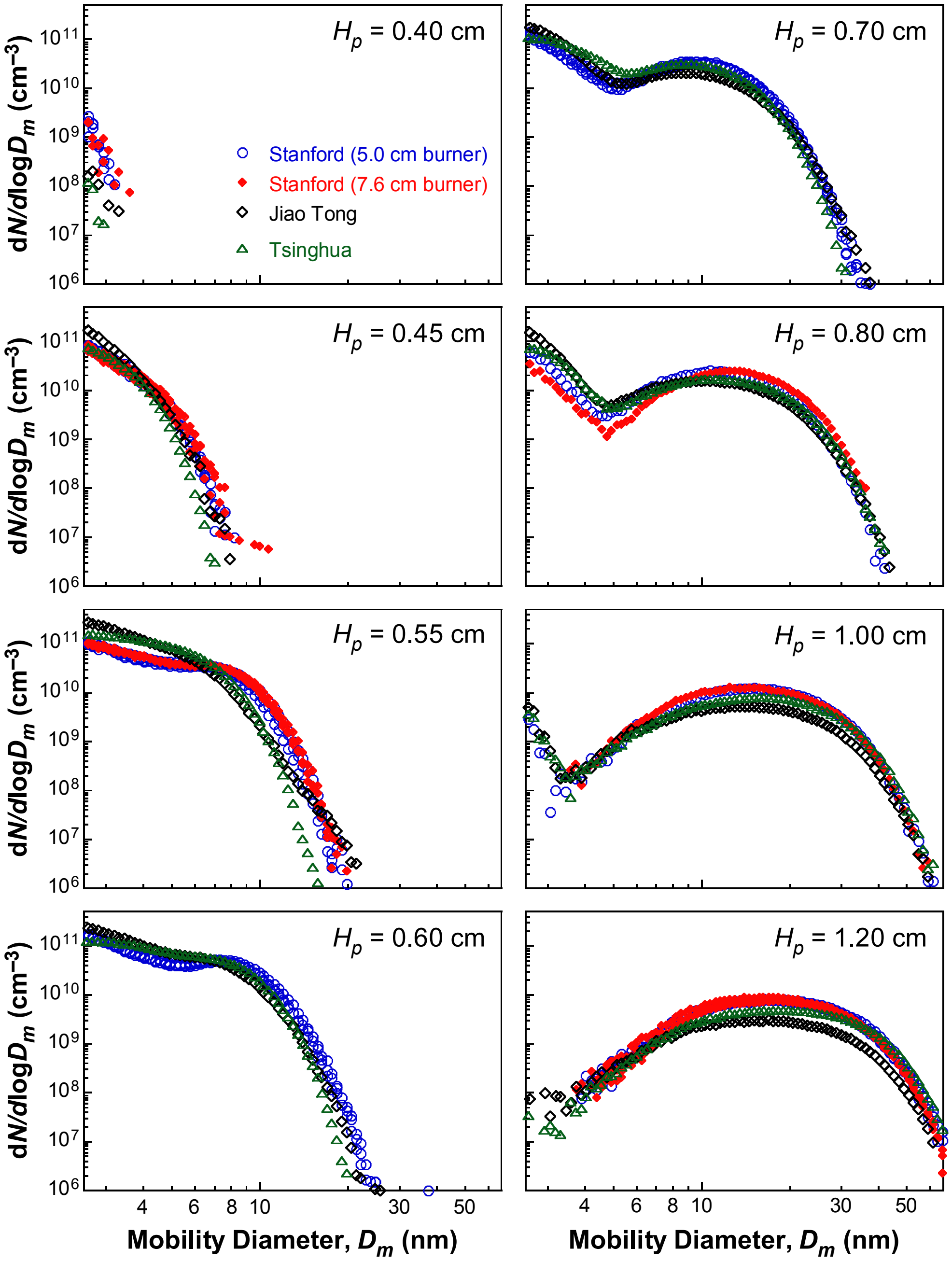

Figure 7. Mobility PSDFs measured at all facilities.

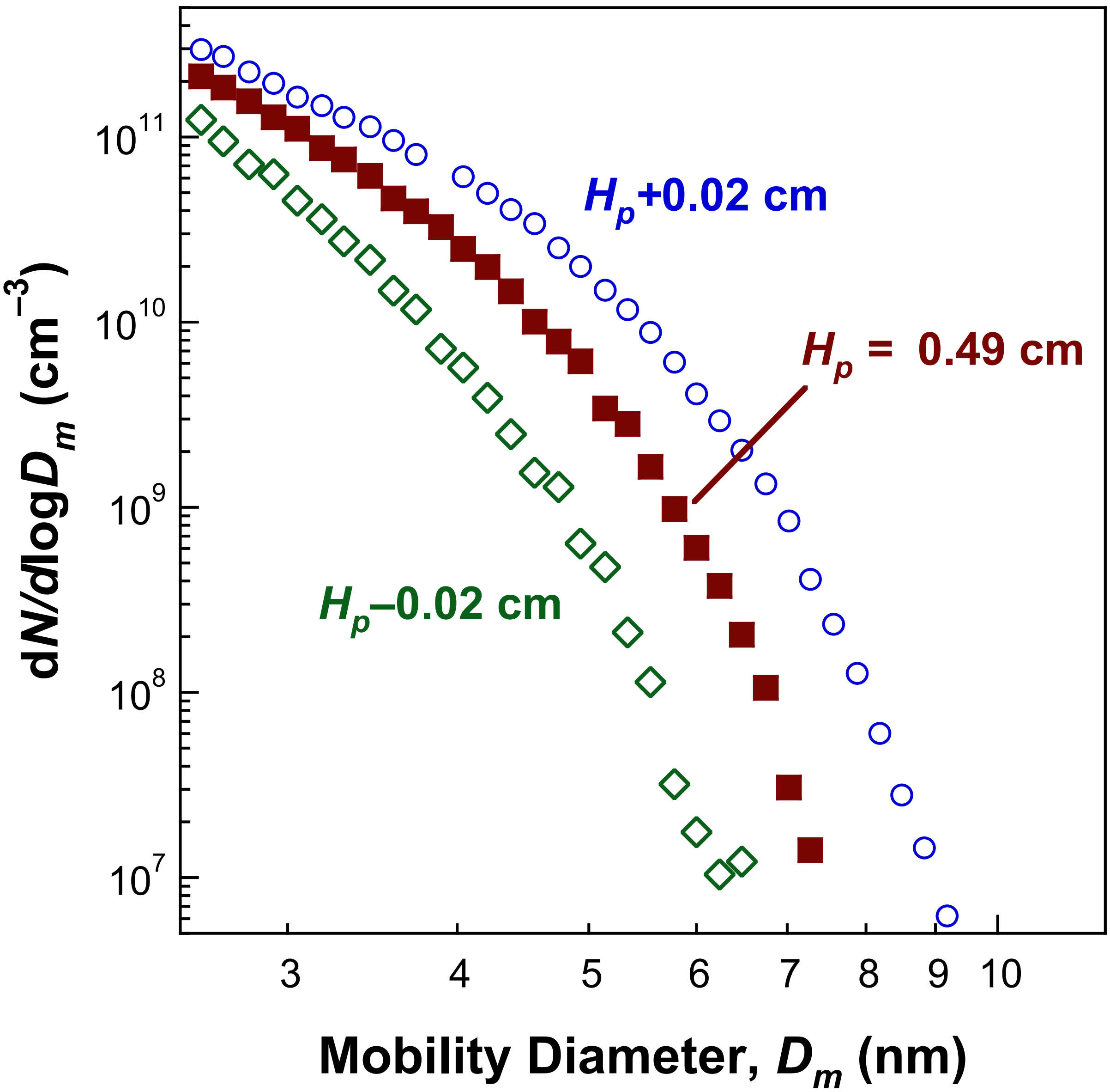

Figure 8. Sensitivity of the mobility PSDF to spatial position during the early soot growth stage. The measurement was done at Shanghai Jiao Tong.

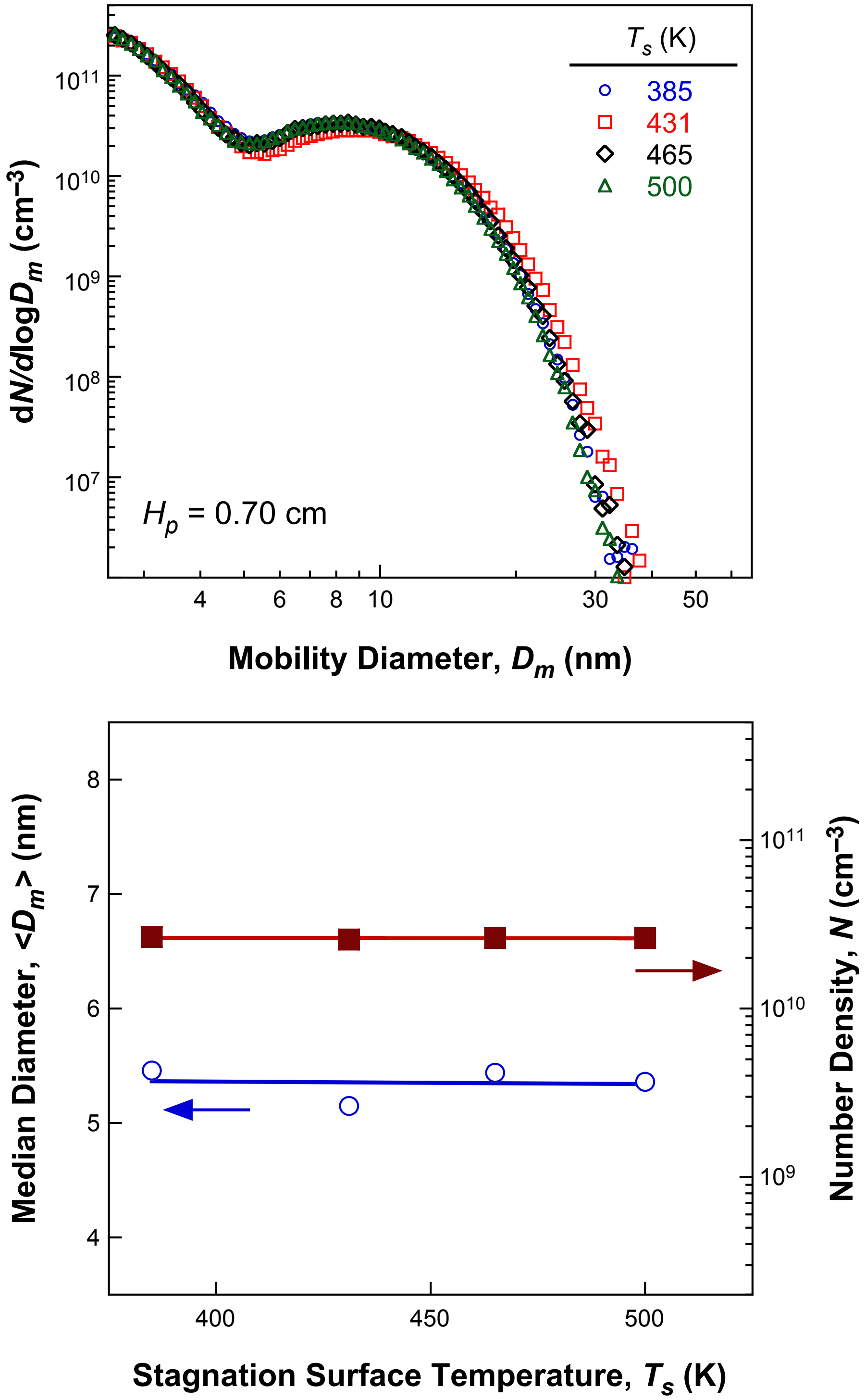

Figure 9. Effect measured for the stagnation surface temperature on the mobility PSDF (top panel) and the median mobility diameter of the PSDF and number density (bottom panel). The measurement was done at Shanghai Jiao Tong.

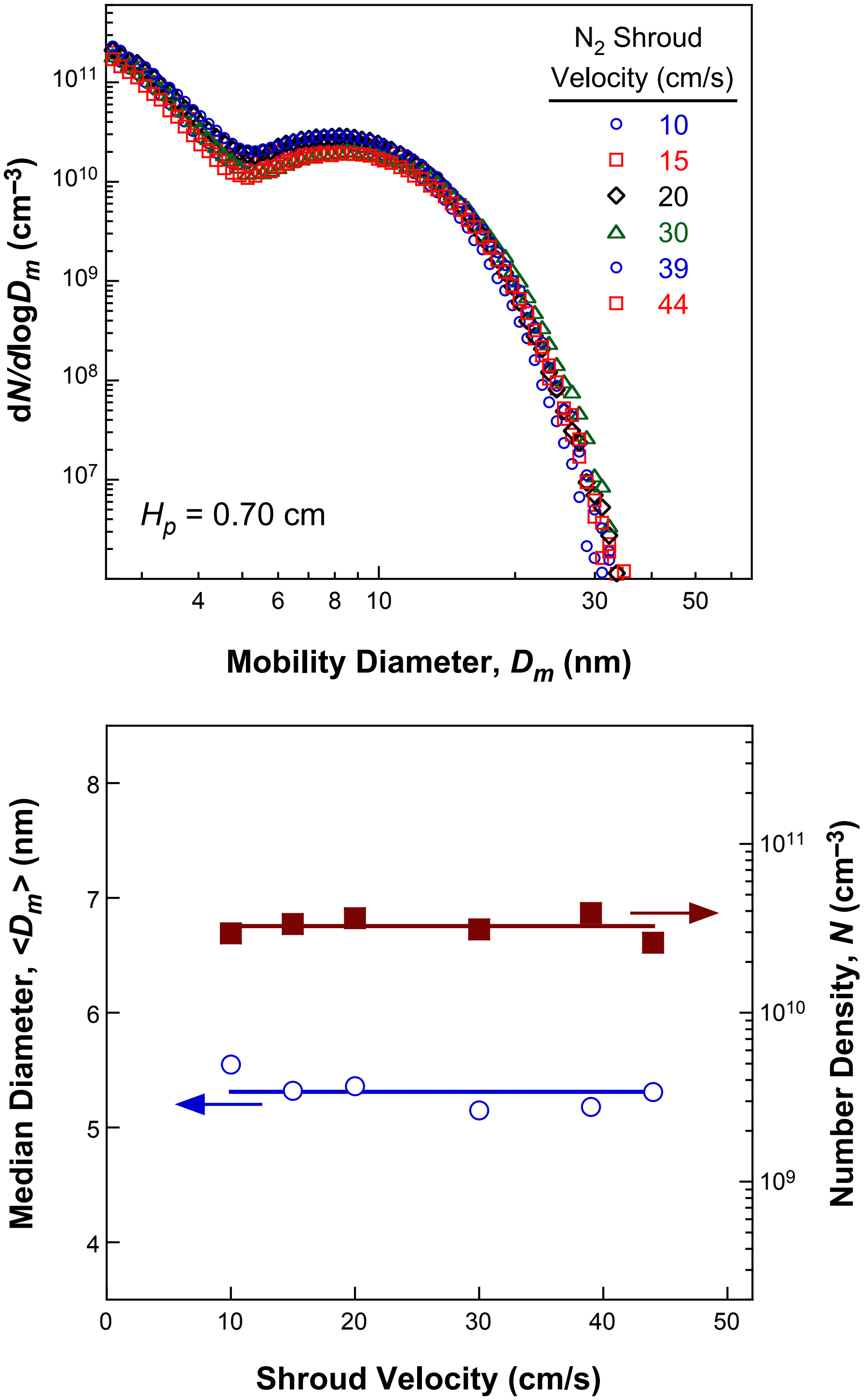

Figure 10. Effect measured for the shroud velocity on the mobility PSDF (top panel), median mobility diameter and number density of the PSDF (bottom panel). The measurement was done at Shanghai Jiao Tong

Click here to download Figure: Figure 11.pdf

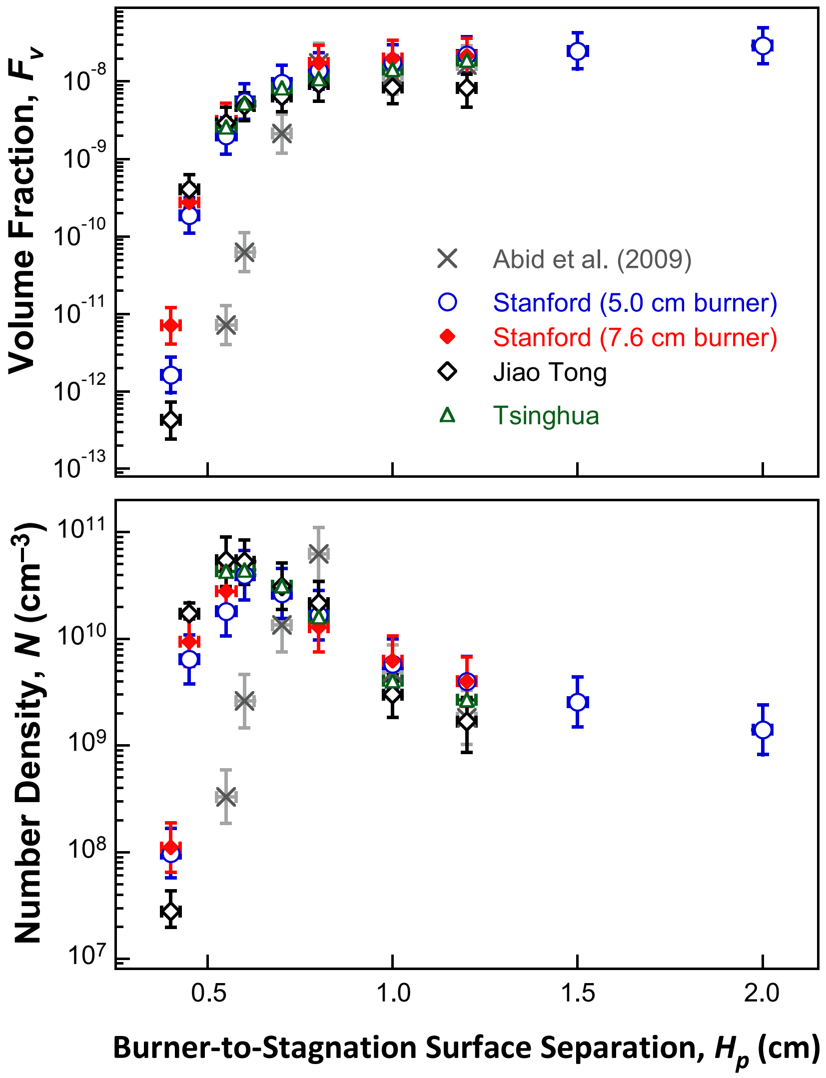

Figure 11. Volume fraction (assuming particle sphericity) and number density from at all facilities as a function of the burner-to-stagnation surface separation, H_p. Experimental uncertainty for each laboratory is shown by the thin, colored error bars and the confidence interval based on the scatter across the facilities and burner sizes is shown as heavy black bars. The volume fraction was calculated from the PSDF assuming particle sphericity.

Figure 12

Click here to download Figure: Figure 12.pdf

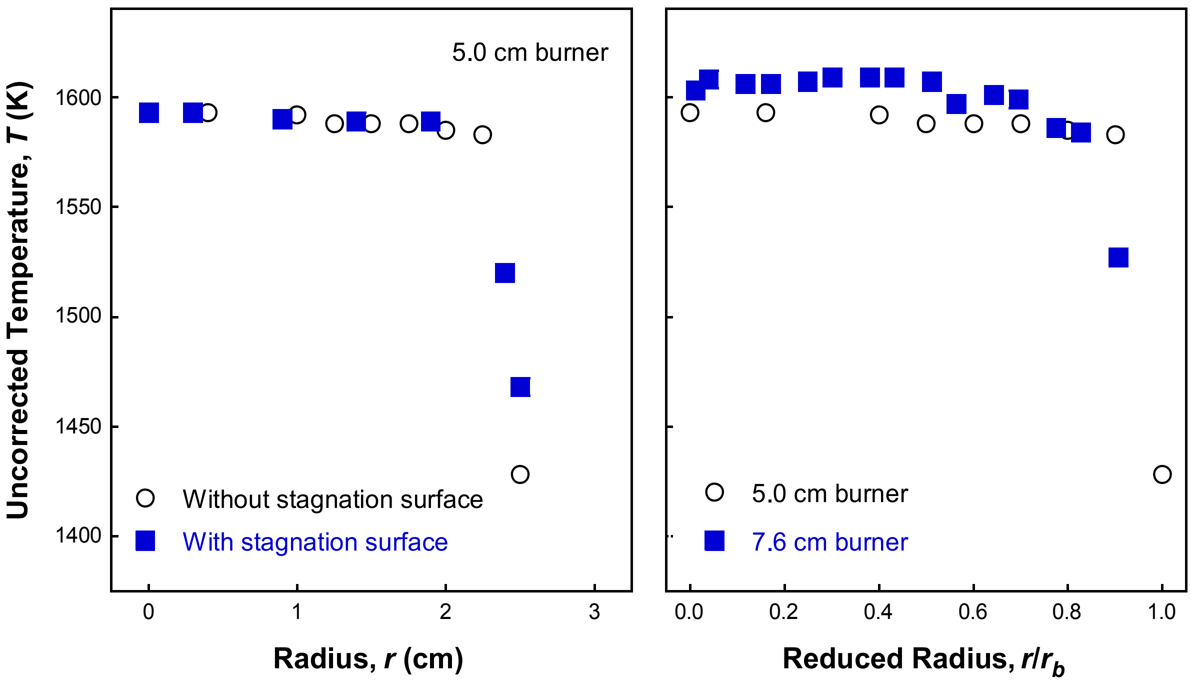

Figure 12. Radial profile of the uncorrected temperature measured at a distance of 0.18 cm from the burner surface for the burner-to-stagnation separation H_p = 1.0 cm, comparing with or without the probe (stagnation surface) (left panel) and for two burner sizes (right panel). The temperature was not corrected for radiation heat loss. The measurement was done at Stanford University.

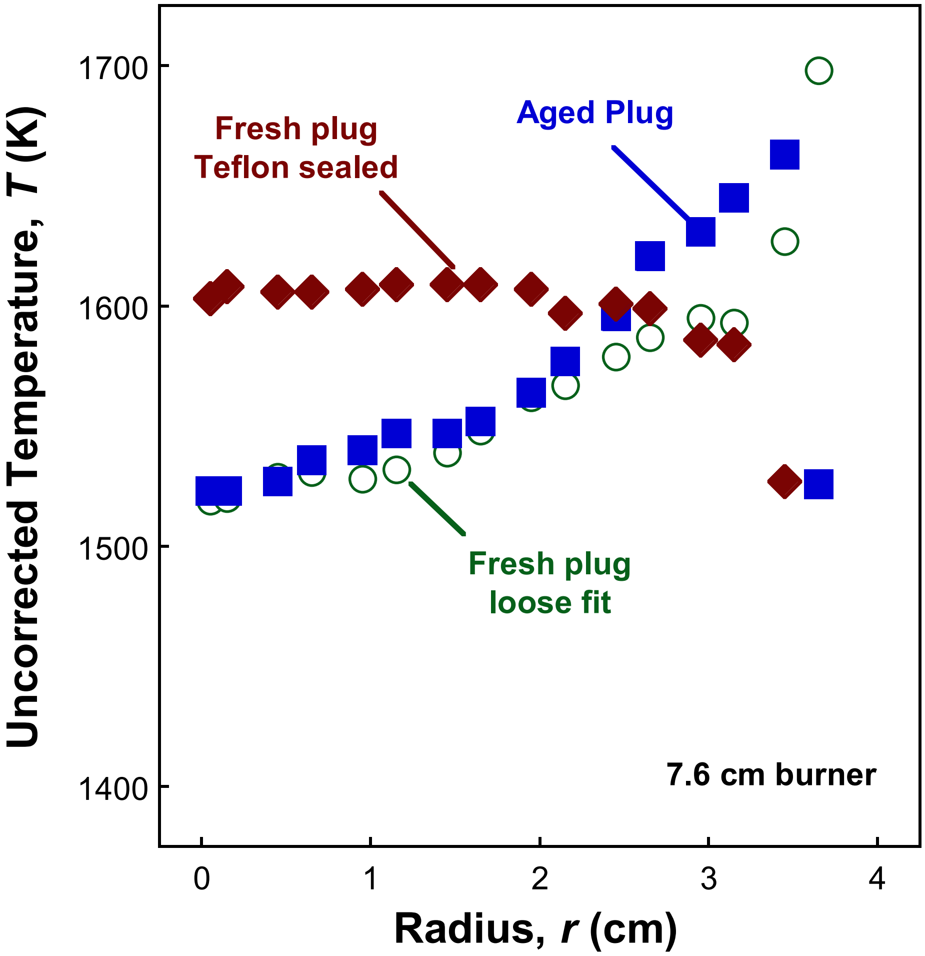

Figure 13. Radial profile of the uncorrected temperature measured at a distance of 0.18 cm from the burner surface for H_p = 1.0 cm, comparing an aged porous plug, a fresh but loose-fitting porous plug and the same fresh porous plug with edges sealed with Teflon tape. The temperature was not corrected for radiation heat loss. The measurement was done at Stanford University.

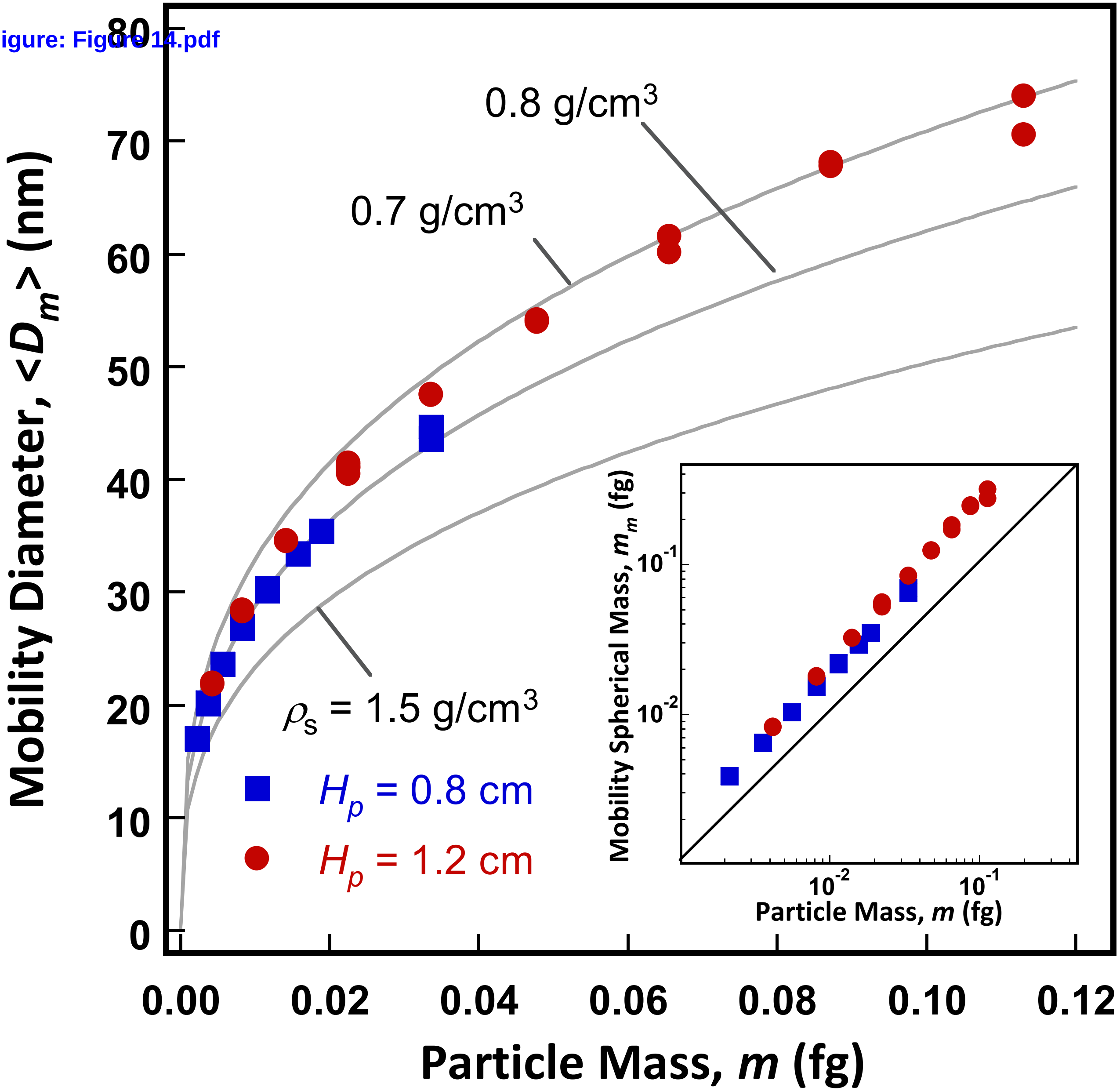

Figure 14. Relationship between the mobility diameter, D_m, and mass, m, measured for particles at two burner-to-stagnation separations (squares: H_p = 0.8 cm, circles: H_p = 1.2 cm), along with a family of curves for spherical particles of varying mass density values. Inset: the mass calculated from mobility diameter assuming sphericity and a mass density of 1.5 g/cm^3 for the particle material (mobility spherical mass, m_m) compared to the actual particle mass measured by CPMA.

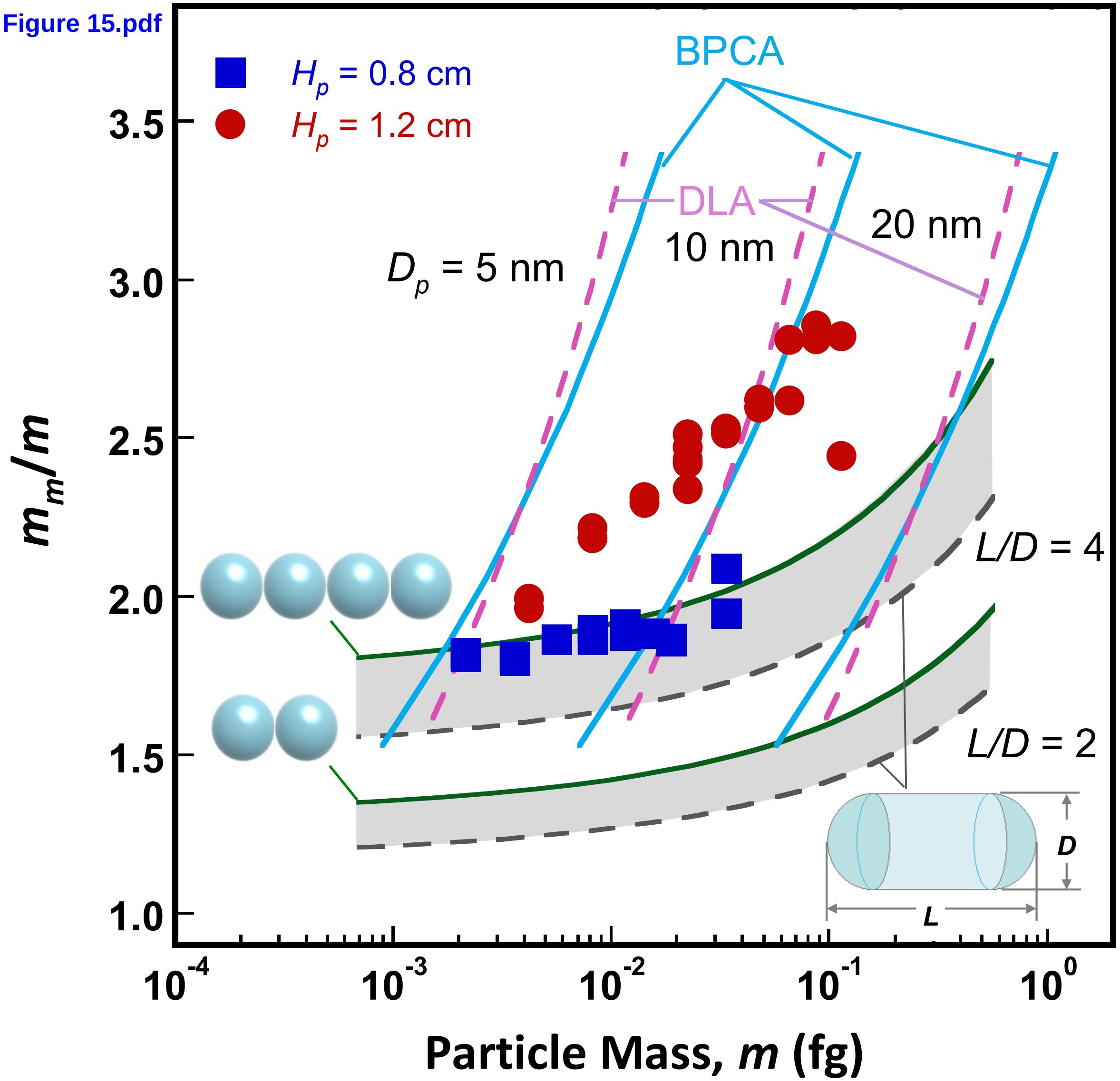

Figure 15. Mobility spherical mass to actual mass ratio as a function of the actual mass, for an assumed mass density of $\rho_s = 1.5$ g/cm^3, comparing the measurements (symbols) and several models (lines) BPCA: ballistic particle-cluster aggregates; DLA: diffusion-limited particle-cluster aggregates; *n*-sphere: aggregates of *n*-primary spherical spheres; and *L*/*D* = *n*: cylinders with spherical caps of length, *L*, and diameter, *D*. The D_p value refers to the diameter of the primary particles in the aggregate. The banded areas indicate shapes that lie between a chain of spheres and a cylinder that are comparable on the basis of equal total lengths and primary particle or cylinder diameters.

Figure 16

Click here to download Figure: Figure 16.pdf

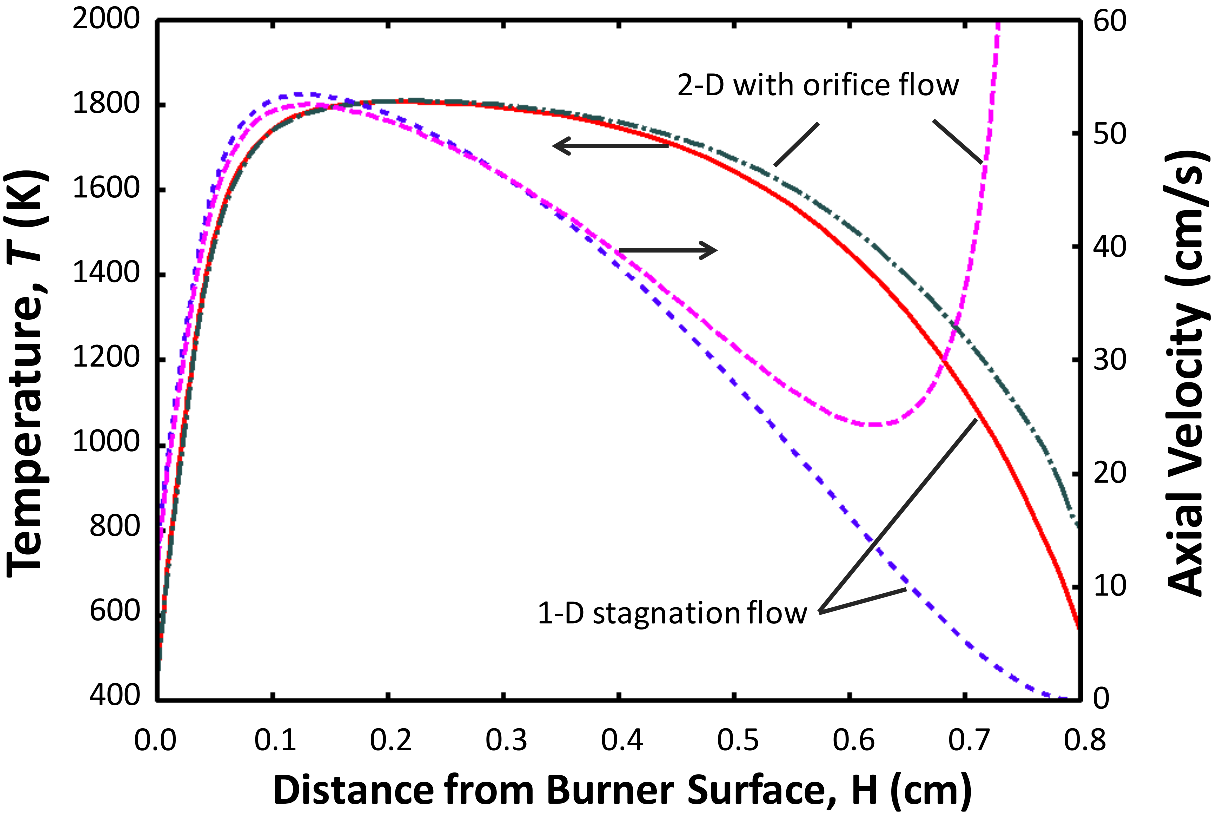

Figure 16. Centerline temperature and axial velocity component computed for the case of $H_p = 0.8$ cm, comparing the results of 1-D stagnation flow calculation and of the centerline of the 2-D simulation with orifice flow.

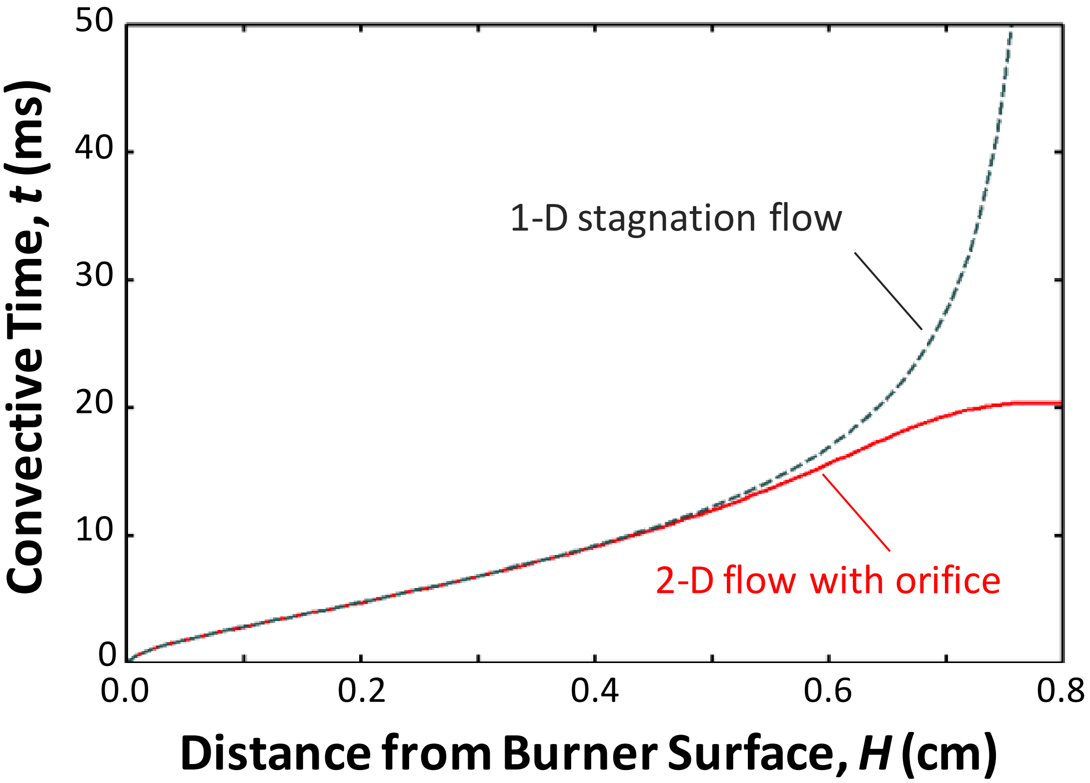

Figure 17. Convective flow time computed for the case of H_p = 0.8 cm, comparing the results of 1-D stagnation flow calculation and of the centerline of the 2-D simulation with orifice flow.